J. Fluid Mech. (1976), *vol.* 74, *part* 2, *pp.* 209–250
Printed in Great Britain

On the two-dimensional mixing region

By F. H. CHAMPAGNE,
Department of Applied Mechanics and Engineering Sciences,
University of California, La Jolla

Y. H. PAO
Flow Research, Inc., Seattle, Washington 98031

AND I. J. WYGNANSKI
School of Engineering, Tel-Aviv University,
Ramat-Aviv, Tel-Aviv, Israel 69978

(Received 25 March 1974 and in revised form 31 July 1975)

An experimental investigation of the two-dimensional incompressible mixing layer was carried out. The measurements provide new information on the development of the mean and turbulent fields towards a self-preserving state and on the higher-order statistical characteristics of the turbulent field. The relevance of initial conditions to the development of the flow is discussed in the light of both present and previous data. Measurements of spectra, probability densities and moments to eighth order of all three velocity-component fluctuations at various transverse positions across the flow were carried out using an on-line digital data acquisition system. The probability density distributions of the derivative and the squared derivative of the longitudinal and lateral velocity fluctuations were also determined. Direct measurements of moments to eighth order of the velocity derivatives were attempted and are discussed in the light of the simultaneously measured histograms. The problems in obtaining higher-order statistical data are considered in some detail. Estimates of the integral time scale of many of the higher-order statistics are presented. The high wave-number structure was found to be locally anisotropic according to both spectral and turbulent velocity-gradient moment requirements. Higher-order spectra to fourth order of the longitudinal velocity fluctuations were measured and are discussed. Finally the lognormality of the squared longitudinal and lateral velocity-derivative fluctuations was investigated and the universal lognormal constant μ was evaluated.

1. Introduction

The two-dimensional incompressible turbulent mixing layer is one of the simplest conceivable free shear flows and one which plays an essential role in many technological problems. A fundamental understanding of the structure of this flow is still far from complete although the general features of the flow were established in 1947 by Liepmann & Laufer. More recently, detailed investigations by Sunyach & Mathieu (1969), Wygnanski & Fiedler (1970), Batt, Kubota

& Laufer (1971), Spencer & Jones (1971), Brown & Roshko (1971), Winant (1972) and Patel (1973) have provided considerable new information and also raised new questions on the structure of the flow. Interesting questions arise from the fundamentally different flow development observed by Liepmann & Laufer (L & L) and by Wygnanski & Fiedler (W & F). W & F speculated that this difference was caused by the presence of a trip wire on the splitter plate in their experiment which was not employed by L & L. Batt *et al.* (1971), in their own experimental facility, were able to reproduce either the L & L or the W & F results, depending on whether a trip wire was used, thereby verifying the important influence of the initial conditions on the development of the flow. Earlier, Bradshaw (1966) had investigated effects of initial conditions on free shear layers. Winant (1972) performed both hot-wire and flow-visualization studies on an undisturbed, but rather low Reynolds number, two-dimensional mixing layer and found considerable evidence for the existence of an orderly process controlling the growth of the layer. This process, termed vortex pairing, involves the interaction of vortices, which form as a result of the shear-layer instability. The vortices were observed to interact pairwise by rolling around each other forming a new single vortical structure of approximately twice the wavelength of the former vortices. Winant's, as well as Brown & Roshko's, observations may shed new light not only on the structure of the mixing layer but also on the effects of initial conditions on the development of the flow.

The higher-order statistical characteristics of turbulent shear flows, and in particular the statistical properties of the small-scale structure are areas where significant data is still lacking. New and higher quality data are required to test the validity and/or limitations of the original universal similarity theory of Kolmogorov (1941) and the later reformulation by Kolmogorov (1962), Oboukhov (1962) and Yaglom (1966). An inherent part of Kolmogorov's theory is the postulate of local isotropy, that is, at sufficiently high Reynolds number, the small-scale turbulent structure is isotropic even when the large-scale structure is not. Convincing experimental support for the postulate is lacking, and evidence for anisotropy of the fine-scale structure in turbulent shear flows is accumulating (see Weiler & Burling 1967; Gibson, Stegen & Williams 1970). Departures from Kolmogorov's original theory have been observed by Gibson *et al.* (1970), Wyngaard & Tennekes (1970) and Van Atta & Chen (1970). Measurements of higher-order spectra and moments of the velocity fluctuations and their derivatives in high Reynolds number flows would provide new information with which to test Kolmogorov's theories.

Frenkiel & Klebanoff (1971) investigated the statistical properties of velocity derivatives in low Reynolds number grid flows and presented data on the moments to eighth order. Tennekes & Wyngaard (1972) pointed out the difficulties in obtaining moments of velocity derivatives in high Reynolds number flows caused by the large dynamic range of the signals and integration time requirements. The difficulties of obtaining such data even at moderate Reynolds numbers in laboratory flows is demonstrated by the results of the present study.

The objectives of the present study are to provide new information on the development of the mean and turbulent fields to a self-preserving state and to

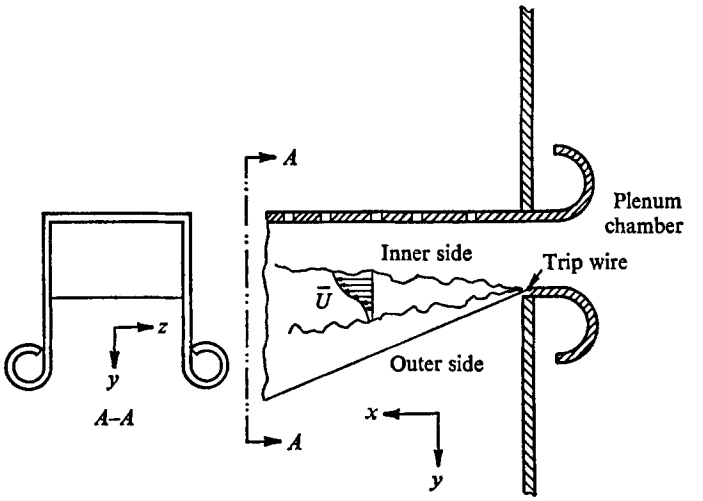

FIGURE 1. Schematic diagram of facility and co-ordinate system.

Co-ordinate	Mean velocity component	R.m.s. turbulent velocity component
x	$\bar{U} = \bar{U}(x, y)$	$\tilde{u}$
y	$\bar{V} = \bar{V}(x, y)$	$\tilde{v}$
z	$\bar{W} = 0$	$\tilde{w}$

present data on the higher-order statistical characteristics for the two-dimensional turbulent shear layer. Particular emphasis is placed on determining the statistical properties of the small-scale structure and providing significant data on the probability densities of the longitudinal and lateral velocity fluctuations and their derivatives. The data presented here were taken before the more recent references were published, and the study was prematurely terminated for reasons beyond the authors' control. The new questions regarding the development of the mixing-layer flow to a self-preserving state will not be settled by the present data, but these data will provide more information on which to base a new study.

2. Experimental apparatus

2.1. *The two-dimensional mixing-layer facility*

A low speed, low turbulence level blower-tunnel was used to supply the flow. A backward step blower powered by a 5 h.p. regulated d.c. motor supplied the air flow through a short diffuser section to a plenum chamber 1·83 m in diameter. The plenum chamber contained two screens and a deep honeycomb in order to reduce the turbulence level at the nozzle exit. The air was exhausted through a rectangular nozzle 17·8 cm wide and 50·8 cm long. The contraction ratio was 28 : 1 and the turbulence level was less than 0·1 %. The flow was allowed to mix on one of its boundaries with the surrounding quiescent air (figure 1), the other three boundaries being solid. To prevent a lengthy transition region, a trip wire was placed just upstream of the mixing region. Eighteen mesh fibreglass

screens were placed about 1·5 m from the open boundary of the test section to help damp out extraneous room drafts. The air was cleaned using a Honeywell electrostatic precipitator, and its temperature did not exceed the ambient room temperature by more than 1 °F. All measurements were made at a nozzle exit speed U_E of 8 m/s. The facility is essentially the same facility used by Wygnanski & Fiedler (1970).

2.2. *Instrumentation*

Velocity fluctuations were measured with Disa type 55D01 constant-temperature anemometers in conjunction with Disa 55D10 linearizers. The linearizers were calibrated to known flow conditions in the free-stream flow of the mixing-layer facility. An overheat ratio of 0·7–0·8 was used for all wires. Lateral-component fluctuations were measured with a symmetric X-array and the lateral-component sensitivities were obtained by yawing the probe $\pm 5°$ in the plane parallel to that of the two wires. The single and X-array hot-wire probes were constructed from 2·3 μm tungsten wire which was copper/gold plated. The active or unplated portion of the wires was about 0·40 mm in length and located in the geometrical centre of the total wire. Typically, the distance between support stems was 3 mm to avoid support-stem flow field disturbances. For X-wire probes, the wires were separated by about 0·4–0·5 mm or one (active) wire length, a value chosen with Wyngaard's (1968) results in mind. The 0·40 mm length corresponds to a length-to-diameter ratio of 175, a minimum value of this ratio required to keep a reasonably uniform temperature distribution (Champagne, Sleicher & Wehrmann 1967). Kolmogorov's length scale η_K is about 0·10 mm in the central region of the flow. No wire-length corrections were applied to the data. The velocity fluctuation signals were differentiated using an analog circuit which consisted of a Philbrick P65AU operational amplifier used as a follower, a Philbrick/Nexus Model 1003 FET operational amplifier used as a differentiator, and two Krohn-Hite Model 330 band-pass filters. One filter was placed at the circuit input to eliminate the high frequency noise from the anemometer and linearizer before differentiation and the other at the circuit output to improve the signal-to-noise ratio and to minimize aliasing. Care was taken to avoid phase shift and amplitude distortion of the signal wave forms. The total phase shift of the overall differentiator circuit was quite linear with frequency over the band of interest. The overall signal-to-noise ratio and the dynamic range, defined as the maximum allowable signal level without distortion or clipping divided by the r.m.s. (or standard deviation σ) of the signal, of the differentiator circuit depends on the signal level encountered, which is a function of position in the flow. For the central region of the flow, typical values are 20 : 1 or 26 dB and $\pm 20\sigma$, respectively. The amplitude response of the differentiator circuit was linear with frequency up to about 12 kHz as the signal was low-pass filtered at 15 kHz. Kolmogorov's frequency f_K, defined as $\overline{U}/(2\pi\eta_K)$, where $\overline{U}$ is the mean velocity, is about 7·5 kHz. The second-derivative circuit had a similar frequency range but the overall signal-to-noise ratio was only 4 and the dynamic range was $\pm 65\sigma$. It should be noted that the noise values used in computations of signal-to-noise ratios were determined for each overall circuit by measuring the output (noise) when the hot wire was

placed in the low turbulence intensity free stream at the same mean velocity as that occurring at the position of interest in the turbulent flow.

Nearly all signal processing was carried out using a direct on-line computer system. Two signals were sent to the computer, the total linearized signal for computing mean velocities and a high-pass filtered version for computing fluctuation quantities; filtering trims off the d.c. component and allows significant amplification to improve resolution. The velocity fluctuation signals were filtered by a Krohn–Hite Model 3340 band-pass filter between 0·10 Hz and 15 kHz. Both the total and filtered signals were sent through Dynamics Model 7514 amplifiers and shielded coaxial cables to an IBM Model 1827 analog-to-digital converter and Model 360-44 computer, the transmission system being free of distortion up to 20 kHz. When derivative signals were to be analysed, the differentiator circuit replaced the Model 3340 filter. The continuous signals were converted to digital samples with a resolution of 14 bits plus a sign bit and the maximum sampling rate was 18000 s^{-1}. The hot wires were normally calibrated directly on-line to determine the overall gain of the system. Analog checks on the mean velocity and turbulence intensity values were consistently carried out in every computer run and excellent agreement with the digital values was always found.

2.3. *Computational techniques*

Spectral measurements were obtained by means of the fast Fourier transform algorithm for time series which is discussed in detail by Cooley, Lewis & Welch (1967). A computer program employing this technique was developed by Pao, Hansen & MacGregor (1969) for on-line processing of turbulence data and was used in this study. The samples were processed in ensembles of 8192, dictated by computer memory requirements as the program performed its operation in-core and retained a running average of the spectral estimates. Typically, from 100 to 300 ensembles (or up to $2{\cdot}5 \times 10^6$ samples) were processed to ensure statistical convergence of the ensemble-averaged spectral estimates, which were monitored through intermediate print-outs. A standard boxcar spectral window of 2·18 Hz was used for all computations and analog checks of several spectral points fell within $\pm$ 10 % of the digital values. Also, the r.m.s. of the fluctuating signals were determined both from the computed spectra and by the usual analog method and the results always agreed to within a few per cent. Higher-order spectra were measured in the same manner as above, only the digitized samples were raised to the appropriate power in the computer before fast Fourier transforming. The first-order or ordinary velocity fluctuation spectra were effectively prewhitened after being sampled by the use of transverse filtering (Blackman & Tukey 1958). The main purpose of prewhitening after the data have been obtained in digital form is to avoid difficulty with the minor lobes of the spectral windows, commonly referred to as a 'spectral leakage'. The result of this leakage problem is to distort the high frequency end of the velocity spectra where the spectral values are five or six orders of magnitude below that of the large-scale energy-containing region. One way of circumventing this problem is to measure the spectrum of the time derivative of the signal and then compute

the spectrum of the signal itself from the appropriate identity relating the two. We chose to do both and compared the results from our measured prewhitened velocity spectrum with the measured (non-prewhitened) velocity-derivative spectrum: excellent agreement was found. The same comparison without prewhitening the velocity spectrum indicated that the spectral estimates of the velocity signal in the region where the spectral values were down roughly six orders of magnitude from the largest values were considerably overestimated by spectral leakage.

Histograms and moments to eighth order were obtained from the high-pass filtered signals. The moments were computed directly from the time series and not from manipulating the histograms or probability density distributions. The signals were sampled at rates of 300–18000 s^{-1}, depending on the nature of the signal, and the data were processed in ensembles of 30000 samples. The effect of sampling rate on the moment estimates is discussed in a subsequent section, but as was expected for stationary random signals, the various sampling rates gave nearly identical results. The estimates of the various moments and the histogram from each ensemble were averaged together with their counterparts from other ensembles to form running means for each moment and the histogram. The running means of the moments were printed out with the on-line printer after each ensemble had been processed to monitor the convergence of the moment estimates. Typically, for a sampling rate of 10^3.s^{-1}, the measured distributions and moments of the velocity fluctuations represent an average of over 30 ensembles or about 10^6 samples and for a total sample length of 10^3 s.

Whenever feasible, the overall on-line system and programs were checked with known signals. For instance, power spectra of first, second, third and fourth order of a sine-wave input signal were determined for various frequencies in the band pass of interest. Similarly, moments to eighth order of sine-wave inputs for various frequencies were measured and excellent agreement with theoretical values were found. Free-stream spectra and moments of the velocity fluctuations and their derivatives were also obtained to determine relevant electronic noise levels in the data.

3. Results and discussion

3.1. *Flow development*

The basic development of the mean velocity profiles is shown in figure 2. Although the same measurements were made previously by Wygnanski & Fiedler (1970) in this apparatus, they were repeated here because the current measurements had to be taken at a lower velocity and some minor changes were made in the apparatus. The profiles appear to be similar from $x = 39{\cdot}5$ cm and to about $x = 80$ cm, where boundary-layer effects from the side wall start to affect the flow field.

The growth of the mixing layer with distance from the step can be estimated from figure 3, which presents the loci of points at which the mean velocity is equal to 0·95, 0·50 and 0·10 of the free-stream velocity. The spread of the mixing layer in the present investigation is nearly the same as that observed by Patel

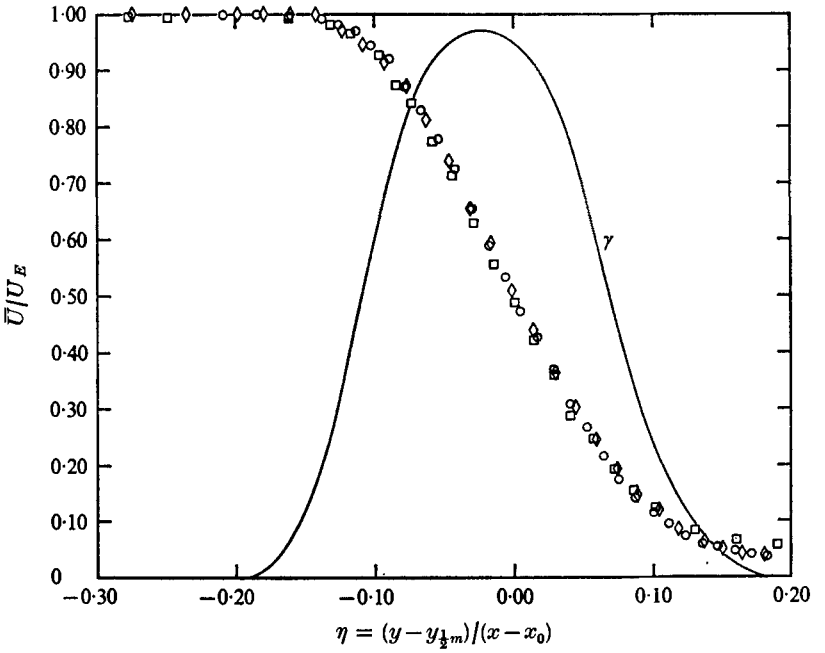

FIGURE 2. Development of mean velocity field. x: ◇, 39·5 cm; □, 49·5 cm; ○, 59·5 cm. γ = intermittency.

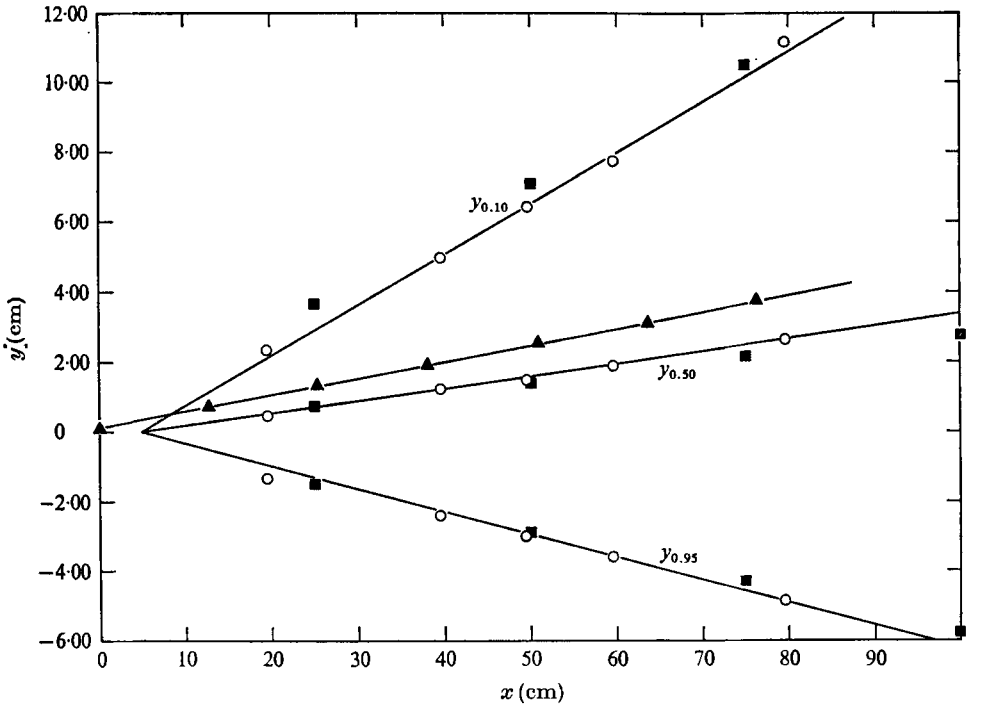

FIGURE 3. The growth of the mixing region with downstream distance. ▲, W & F; ■, Patel; ○, present results.

Author	x_0 (cm)	$Re_{x\,\max}$	$\frac{y_{0.5}-y_{\text{plate}}}{x-x_0}$	$\frac{y_{0.95}-y_{0.1}}{x-x_0}$
Liepmann & Laufer (1947)	0	9×10^5	0·031	0·17
Wygnanski & Fiedler (1970)	−1·9†	5×10^5	0·048†	0·23†
Batt *et al.* (1970)	6	6×10^5	0·06	0·17
	−4·3†		0·07†	0·23†
Spencer & Jones (1971)	0	1×10^6	0·04	0·19‡
Patel (1973)	−1·9	2×10^6	0·027	0·19
Present study	5	4×10^5	0·035	0·208
Batt (1974)	6	6×10^5	—	0·22

† Trip wire used.

‡ Obtained by assuming an error-function profile with $\sigma = 11$ as the authors did not show an experimental velocity profile for this case.

TABLE 1

(1973) and Liepmann & Laufer (1947), and is somewhat less than that in the corresponding flow reported by Wygnanski & Fiedler (1970). The latter difference is attributed to the failure of the trip wire to trigger transition and produce a turbulent boundary layer. A hot wire was traversed near the step downstream of the trip wire and it was indeed observed that the flow although disturbed was not turbulent. Table 1 provides a comparison of the various spreading parameters reported for a uniform flow mixing with quiescent surrounding fluid. The second column shows the effect of a trip wire on the location of the hypothetical origin of the flow relative to the position of the step or discontinuity. The virtual origin x_0 for a tripped mixing layer occurs upstream of the step or discontinuity while that for an untripped flow occurs predominantly either at the step or downstream from it. The actual value of x_0 depends on the thickness of the initial boundary layer and the nature of the disturbances present in the boundary layer (Bradshaw 1966; Batt *et al.* 1970). The fourth column gives the slope of the locus of points at which the velocity is equal to half the free-stream velocity, i.e. the $\eta = 0$ line. These data could be representative of the spread of the mixing layer if it were not so sensitive to the angle between the flow direction and the alignment of the splitter plate upstream of the discontinuity. The relatively large values of $(y_{0.5}-y_{\text{plate}})/(x-x_0)$ which were observed by Batt *et al.* (1970) can be attributed to a 1° flow angularity in their apparatus.† In general

$$0{\cdot}03 \leqslant (y_{0.5}-y_{\text{plate}})/(x-x_0) \leqslant 0{\cdot}04$$

for untripped mixing layers and

$$0{\cdot}04 \leqslant (y_{0.5}-y_{\text{plate}})/(x-x_0) \leqslant 0{\cdot}05$$

for disturbed or tripped mixing layers. The most sensible measure of the growth of the mixing layer is the local width of the flow $(y_{0.95}-y_{0.10})/(x-x_0)$ because it is independent of most extraneous parameters. It was shown by Batt *et al.* (1970) that placing a trip wire upstream of the discontinuity altered the value

† Private communication from R. G. Batt.

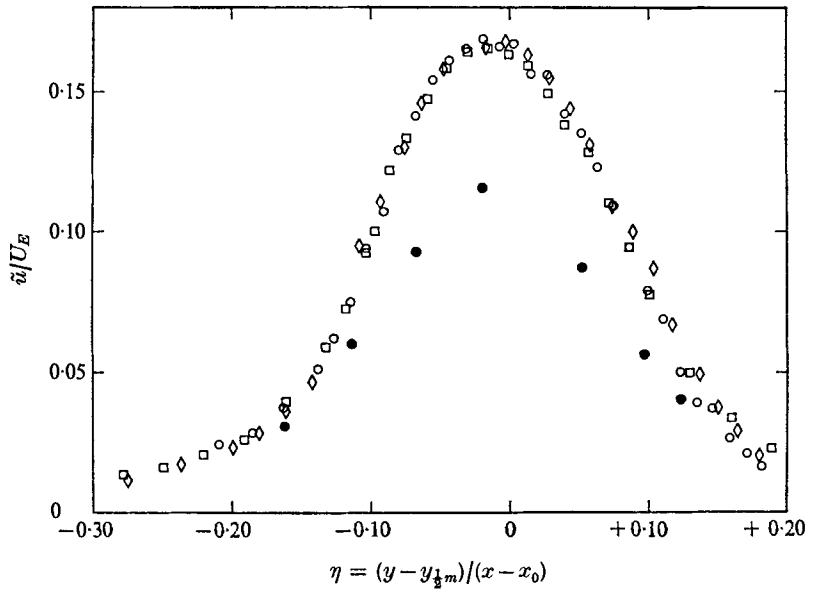

FIGURE 4. The distributions of the longitudinal velocity fluctuation $\tilde{u}$ and the lateral velocity fluctuation $\tilde{v}$. $\tilde{u}$: ◇, x = 39·5 cm; □, x = 49·5 cm; ○, x = 59·5 cm. $\tilde{v}$: ●, x = 59·5 cm.

of $(y_{0\cdot95} - y_{0\cdot10})/(x - x_0)$ from 0·17 to 0·22; the former number is in agreement with the observations of Liepmann & Laufer (1947) while the latter agrees with the tripped data reported by Wygnanski & Fiedler (1970). In the present investigation an intermediate spreading angle was observed, perhaps because of the disturbance which was imposed on the boundary layer just upstream of the step. The present data are in agreement with the results of Patel (1973) and of Spencer & Jones (1971), although in the latter case the agreement may be fortuitous since the value of $y_{0\cdot95} - y_{0\cdot1}$ was derived by assuming that the velocity profile is well represented by an error function. Patel (1973) did not describe the state of the initial boundary layer on the splitter plate for his experiment. However the initial boundary layer in Patel's blower cascade wind tunnel was studied by Wygnanski & Gartshore (1963), who found that the boundary layer was undergoing transition. Thus Patel's initial conditions were somewhat similar to those in the present experiment, a disturbed but not fully turbulent state. The mean velocity profile is given in figure 2 and is in agreement with all previous investigations provided one chooses the appropriate spreading parameters. The intermittency distribution γ, which is also shown in figure 2, was measured previously (Wygnanski & Fiedler 1970) for U_E = 12 m/s. This distribution is shown merely to give a rough idea of the intermittency at any position in the flow.

The distributions of the longitudinal turbulence intensity at three downstream locations is shown in figure 4. These results indicate that the $\tilde{u}$ distributions are self-preserving beyond x = 39·5 cm, or correspondingly $Re_x \approx 2{\cdot}2 \times 10^5$, which is somewhat lower than the corresponding values reported by Liepmann & Laufer or Wygnanski & Fiedler. Also shown in figure 4 is the distribution of

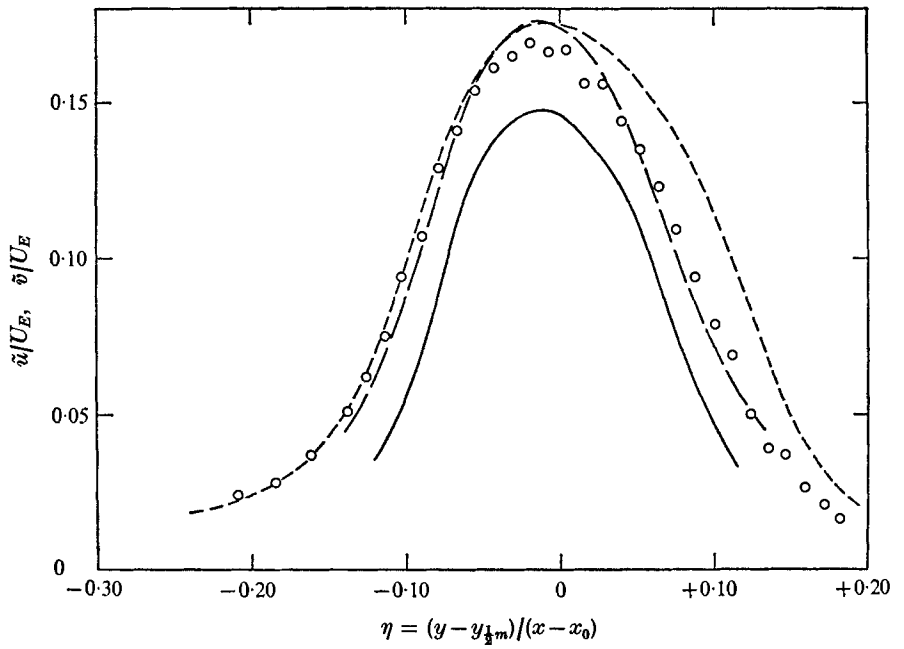

FIGURE 5. Comparison of longitudinal turbulence intensity distributions. ○, present; ——, Liepmann & Laufer; – – –, Wygnanski & Fiedler; — —, Patel.

the lateral turbulence intensity $\tilde{v}$ at $x = 59{\cdot}5$ cm, which is the location at which all subsequently described measurements were carried out. In view of the differences in spreading rate discussed above, it was felt that it might be instructive to compare the turbulence intensity distributions obtained by Liepmann & Laufer, Wygnanski & Fiedler and Patel with the present results. Although other studies of the mixing layer have been recently carried out by Castro (1973) and Batt (1974), comparison will be made only with Wygnanski & Fiedler's (1970) and Patel's (1973) results, the latter as they represent the largest Reynolds number results available. The $\tilde{u}$ profiles are shown in figure 5 and it is readily apparent that Liepmann & Laufer's results are considerably lower in magnitude, either because of inadequate anemometer response or because of a lower initial disturbance level (Batt *et al.* 1970). The other profiles appear to collapse together on the high velocity side of the flow field, whereas for $\eta > 0$ the Wygnanski & Fiedler results appear to deviate from these distributions. It would appear from the $\tilde{u}$ results that the increased spreading observed by Wygnanski & Fiedler occurs entirely on the low velocity side of their mixing layer. The $\tilde{v}$ profiles shown in figure 6 indicate better agreement between the profiles on the low velocity side of the flow, although the degree of the agreement is less than that observed in the $\tilde{u}$ profiles on the high velocity side. The present data agree with Patel's results quite well while the Wygnanski & Fiedler data indicate higher intensities on the high velocity side. As the w statistics were measured at only four positions across the flow, the results for $q^2 = \frac{1}{2}(\overline{u^2}+\overline{v^2}+\overline{w^2})$, normalized by U_E^2, are tabulated in table 2 along with the

η	Present results	W & F	Patel
−0·113	0·0055	0·0112	0·0055
−0·019	0·029	0·036	0·027
+0·052	0·0165	0·0205	0·0145
+0·097	0·0055	0·0094	0·0063

TABLE 2. $\dfrac{q^2}{U_E^2} = \dfrac{1}{2}\left(\dfrac{\overline{u^2}+\overline{v^2}+\overline{w^2}}{U_E^2}\right)$

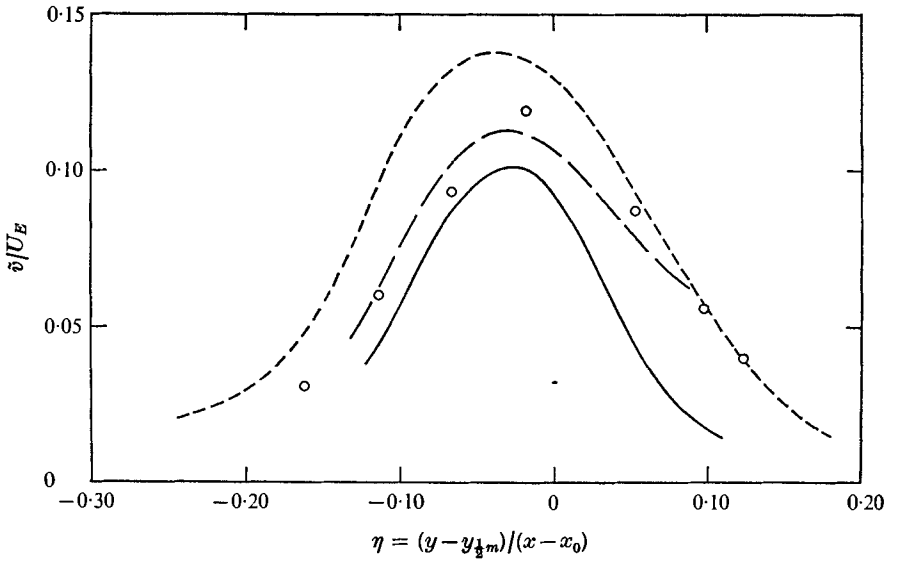

FIGURE 6. Comparison of lateral turbulent intensity distributions. ○, present; ——, Liepmann & Laufer; – – –, Wygnanski & Fiedler; — —, Patel.

corresponding values obtained by Wygnanski & Fiedler and Patel. Thus the present data are in general agreement with the highest Reynolds number data available, those of Patel (1973), in nearly all respects. In considering the Wygnanski & Fiedler (1970) results, one must keep in mind the Batt *et al.* (1970) study, where the $\overline{U}$ and $\tilde{u}$ distributions for both a tripped and 'partially' tripped (i.e. their trip wire also did not trigger complete transition in the initial boundary layer) mixing layer were measured. They reported that their untripped case nearly reproduced the Liepmann & Laufer $\tilde{u}$ distribution, while their results for the partially tripped case are quite similar to the Wygnanski & Fiedler $\tilde{u}$ distribution (and nearly identical to the corresponding present distribution). Their mean velocity distributions indicated good agreement with Liepmann & Laufer's for the untripped case, while for the tripped case they found agreement with Wygnanski & Fiedler's results (see also table 1). Thus the difference in the distributions shown in figures 5 and 6 indicate real effects caused by the state of the initial boundary layer and can not be attributed to inadequacies in the measurement technique. Batt *et al.*, therefore, showed that for the same Reynolds number, two different growth rates were possible depending on the initial

conditions. A reasonable speculation based on the above data is that the spread or width of the mixing layer as well as the magnitude of the peak in the intensity profile is proportional to the disturbance level of the initial boundary layer on the splitter plate (Bradshaw 1966).

At this point one might rightfully ask whether there exist in the two-dimensional mixing layer *universal* self-preserving distributions of the mean velocity, turbulence intensities and other mean quantities not determined by viscous effects. According to the principle of Reynolds number similarity/independence, these self-preserving distributions should be universal.

In reply, two alternatives seem plausible. One is that no *universal* self-preserving form exists although each mixing layer in itself is self-preserving, the self-preserving functions being dependent on the initial conditions of the flow. Winant (1972) proposes a vortex-pairing model of the mixing layer developing from an undisturbed initial boundary layer and the model seems to fit his experimental observations. Vortex pairing implies a kind of orderly structure in the flow and perhaps this model is applicable to the untripped mixing layer of Liepmann & Laufer. A reasonable conjecture would be that if the initial boundary layer is highly disturbed or even turbulent the orderly vortex-pairing process might occur randomly, in some intermittent fashion or not at all. Then this pairing process would not govern the growth of the mixing layer and a different growth rate would undoubtedly be observed. In other words, one might expect that the instability problem and subsequent flow development could be different for an initially laminar mixing layer and for an initially turbulent mixing layer. In any case, the initial state of the boundary layer plays a strong role in the development of the flow, perhaps through the modification of some orderly process like that proposed by Winant. It was also noted that the initial mixing layer of an axisymmetric jet was affected by disturbances introduced in the exit flow (Crow & Champagne 1971). For example, the frequency of the disturbance has a strong effect on the growth of the mixing layer.

The second alternative is that it is not the initial conditions which are so important, but rather the boundary conditions. This alternative has been suggested by Laufer & Browand (private communication). They are concerned primarily with the boundary conditions imposed by the end plates. Browand has experimentally observed that if the ratio of the spatial distance between adjacent vortex structures to the distance between the end plates is of the order of $\frac{1}{4}$ or larger, a strong inflow from the side-wall boundary layers into the core of the vortices occurs. As a result, the magnitudes of the fluctuations increase as well as the entrainment rate. They postulate that, as the initial shear-layer thickness is increased by the presence of a trip wire, the above condition is satisfied at an earlier stage of development of the mixing layer and may explain the Wygnanski & Fiedler and Batt *et al.* results.

It is difficult to assess the validity of either alternative, although it should be pointed out that Patel used a 50 % larger end-plate separation than was used in he present experiments and the results agree quite well as shown previously. Until systematic experiments are carried out to investigate the importance of initial conditions and end-plate separation at high Reynolds number (i.e. $Re_x \approx 10^6$),

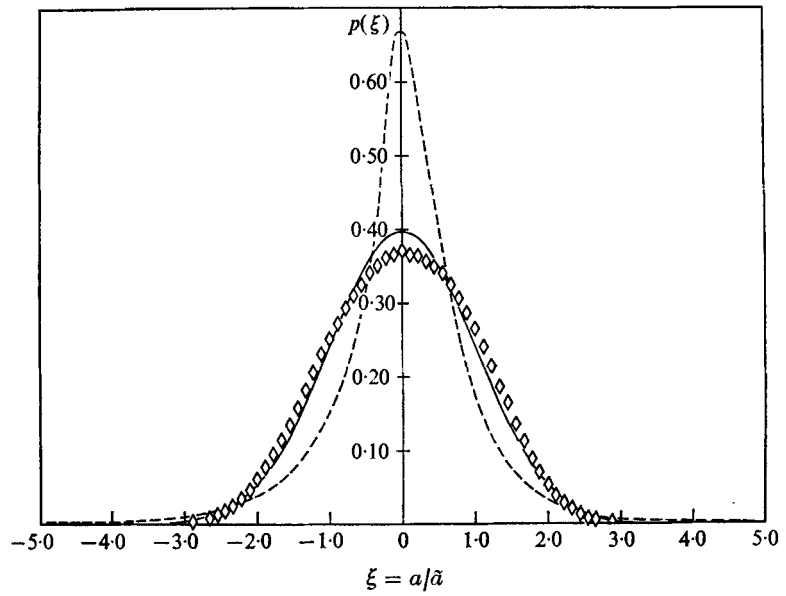

FIGURE 7. Measured probability density distributions of u and $\partial u/\partial t$ at $\eta = -0{\cdot}019$. ◇, u; – – –, $\partial u/\partial t$; ——, normalized Gaussian.

there is no definitive basis for an answer. It is hoped that the information and discussion presented here will prove valuable in designing new experimental studies.

3.2. *Probability densities and higher-order moments*

Measurements of the probability densities and moments to eighth order were carried out for all three components of the velocity fluctuations at various transverse positions across the flow at $x = 59{\cdot}5$ cm. Similar measurements of the first derivative of the longitudinal component were made but moments to only fifth order could be reliably determined as will be discussed below.

Figure 7 shows the measured probability density distribution of the u signal and its derivative taken at $\eta = -0{\cdot}019$, which is approximately the centre of the u distribution. The random variables in all probability density plots have been normalized by their variance. The probability density shown in all plots is the normalized density defined by

$$P(\xi) = \tilde{a}P^*(a),$$

where $\xi = a/\tilde{a}$ for the random variable a. In the centre of the mixing layer, where the lateral mean strain rate is at a maximum, the probability density is nearly Gaussian, as is observed in homogeneous grid turbulence and on the centre-line of an axisymmetric jet (Kuo & Corrsin 1972), where the mean strain rate is zero. The u distribution is characterized by a skewness of $-0{\cdot}04$ and flatness factor of 2·6. The first-derivative signal has a skewness and flatness factor of $+0{\cdot}5$ and 10·4 respectively, while for the second derivative they are $-0{\cdot}06$ and 37. Thus the higher the derivative the more the probability density differs from the normal distribution. This was observed also by Kuo & Corrsin (1972), who showed

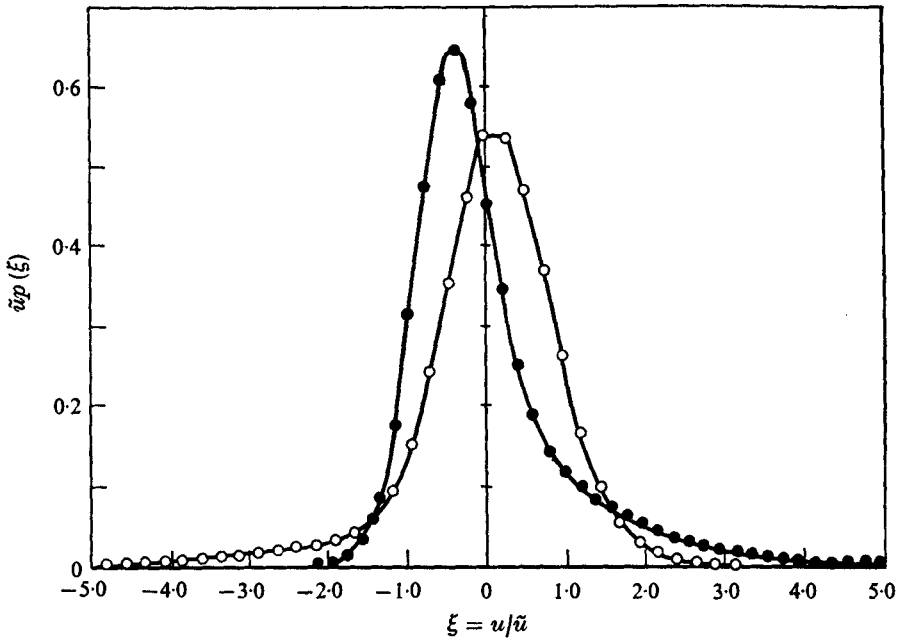

FIGURE 8. Measured probability density distributions of u.
○, $\eta = -0{\cdot}092$; ●, $\eta = +0{\cdot}143$.

further that the deviation from normality increased with increasing Reynolds number. The nature of the deviation for the derivative signals is a higher probability than the normal density for small amplitude values and features that characterize an intermittent signal at very large amplitudes.

The measured u probability densities at approximately the two half-turbulence-intensity points are shown in figure 8. The probability density for the low velocity side exhibits a peak at a small negative amplitude, has a long tail at large positive amplitudes, and is characterized by a skewness of $+1{\cdot}7$. The peak at small negative values of u is most likely caused by potential fluctuations, and the tail at large positive values by large turbulent bulges or eddies. This is consistent with visual observation of oscilloscope traces and figure 7 in Wygnanski & Fiedler (1970). The density distribution for the high velocity side shows just the opposite behaviour, although its peak is not displaced from zero amplitude so much and its skewness is $-1{\cdot}5$.

The measured v-component probability density distributions at the centre of the flow and the two half-intensity points are shown in figure 9. The distribution for the high velocity side shows a peak at small positive values of $v/\tilde{v}$, which can be attributed to the potential fluctuations, and a large tail for negative $v/\tilde{v}$, which is caused by the large amplitude negative fluctuations carried by the large eddies or turbulent bulges. This interpretation is consistent with the results shown in figures 41 and 42 in Wygnanski & Fiedler. The skewness of this distribution is $-1{\cdot}1$. Again the opposite behaviour is exhibited by the distribution on the low velocity side, whose skewness is $+1{\cdot}1$. In the centre of the flow, the density is not quite Gaussian and has a skewness of $-0{\cdot}08$ and a flatness factor

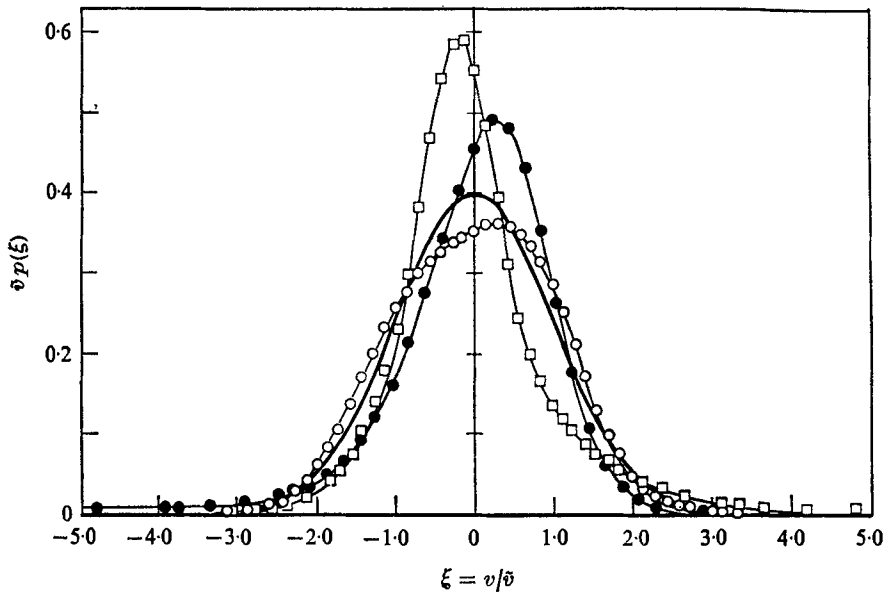

FIGURE 9. Measured probability density distributions of v. ○, $\eta = -0{\cdot}113$; ●, $\eta = -0{\cdot}019$; □, $\eta = +0{\cdot}097$; ——, normalized Gaussian.

of 2·6. The corresponding statistics for the derivative of the v signal at the same location are $-0{\cdot}04$ and 13·6. Note that the sign of the skewness of v is consistent with an outward growth of the mixing layer on both sides of the flow. Corrsin (1950) related the skewness of the probability density of v to the lateral gradient of the v-component intensity for fully turbulent, non-intermittent flow. Although this model appears plausible in view of the present data, no detailed comparison was carried out because of the strong effect of intermittency on the v statistics.

Figure 10 shows the w probability density distributions for the centre and two half-intensity points. The distribution is nearly Gaussian in the centre of the flow, as would be expected from the flow symmetry in z, and the skewness and flatness factors are $-0{\cdot}010$ and 3·07, respectively. The distributions at the two half-intensity points deviate considerably from a normal distribution and this can undoubtedly be attributed to intermittency effects. On the low velocity side of the flow the distribution has a skewness of $+0{\cdot}27$ and a flatness factor of 7·02 while the corresponding values for the high velocity side of the flow are $-0{\cdot}20$ and 12·1. The observed behaviour of the w distributions, as well as that of the u and v distributions, agrees qualitatively with similar distributions measured by Spencer (1970) in a mixing layer between two streams with a velocity ratio r of 0·6.

Table 3 presents the values of the various moments of the u, v, w, $\partial u/\partial t$, $\partial v/\partial t$ and $\partial^2 u/\partial t^2$ signals measured at $\eta = -0{\cdot}019$. These moments were computed directly from the time series and not by using the probability density distributions. Before presenting further results on the distributions of the higher-order moments across the flow, it is appropriate at this point to consider the magnitude of the mean relative error in the moment estimates for the integration times used and possible effects of the chosen sampling frequencies on the estimates

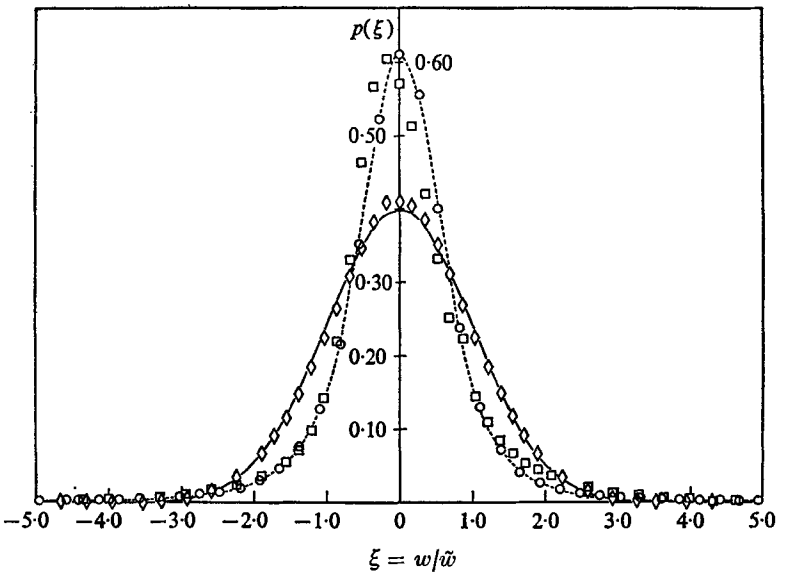

FIGURE 10. Measured probability density distributions for w. ◇, $\eta = 0{\cdot}019$; ○, $\eta = 0{\cdot}113$; □, $\eta = 0{\cdot}097$; ——, normalized Gaussian.

a	$\overline{a^3}/\tilde{a}^3$	$\overline{a^4}/\tilde{a}^4$	$\overline{a^5}/\tilde{a}^5$	$\overline{a^6}/\tilde{a}^6$	$\overline{a^7}/\tilde{a}^7$	$\overline{a^8}/\tilde{a}^8$
u	−0·035	2·60	−0·16	10·2	−0·27	52
v	−0·081	2·59	−0·47	10·4	−0·03	57·4
w	−0·010	3·07	−0·10	15·5	−1·03	107
$\partial u/\partial t$	0·50	10·4	21·2	541	1633	$8{\cdot}3\times10^4$
$\partial v/\partial t$	−0·039	13·6	−3·7	725	−432	$7{\cdot}3\times10^4$
$\partial^2 u/\partial t^2$	−0·06	37·4	127	$1{\cdot}4\times10^4$	—	—

TABLE 3

of the various moments. The distributions of the integrands of the moments of the signals, especially the derivative signals which have rather large kurtosis values, will be examined to ensure that the dynamic range of the processing circuits was adequate (Tennekes & Wyngaard 1972). Tennekes & Lumley (1972) showed that the mean-square relative error $\epsilon^2(\bar{a})$ in the mean value $\bar{a}$ of a stationary random signal a determined by integration over a period of time T is given by

$$\epsilon^2(\bar{a}) = (\overline{[a-E(a)]^2}/[E(a)]^2)\,2\tau/T, \tag{1}$$

where $E(a)$ is the expected value of the stationary random variable a and τ is the integral time scale of a.

Application of (1) to the determination of the variance σ^2, the skewness S or M_3, and the fourth moment M_4 or K gives

$$\left.\begin{aligned}\epsilon^2(\sigma^2) &= (K-1)\,2\tau_2/T,\\ \epsilon^2(S\sigma^3) &= (M_6/S^2-1)\,2\tau_3/T,\\ \epsilon^2(K\sigma^4) &= (M_8/K^2-1)\,2\tau_4/T,\end{aligned}\right\} \tag{2}$$

where τ_n is the integral time scale of the nth moment. The formulation (1) is useful *a priori* only if reasonable estimates of high-order moments and integral time scales are available. The integral time scale of a stationary random function is defined to be the integral of the autocorrelation coefficient:

$$\tau_n = \frac{1}{\overline{r_n^2}} \int_0^\infty \overline{r_n(t)\, r_n(t+\tau)}\, d\tau = \frac{1}{R_n(0)} \int_0^\infty R_n(\tau)\, d\tau, \tag{3}$$

where $r_n(t)$ is a stationary random function with zero mean. For the case $n = 1$, $r_1(t) = a(t)$, while in general $r_n(t) \equiv a^n(t) - \overline{a^n}$. The integral scale can be inferred from the value of the spectrum function $E_n(\omega)$ evaluated at zero frequency, where $E_n(\omega)$ is defined as

$$E_n(\omega) = \frac{2}{\pi} \int_0^\infty R_n(\tau) \cos(\omega\tau)\, d\tau. \tag{4}$$

Thus, for $\omega = 0$,

$$\tau_n = \frac{\pi}{2} \frac{\lim_{\omega \to 0} E_n(\omega)}{\overline{r_n^2}} = \frac{\pi}{2} \frac{\lim_{\omega \to 0} E_n(\omega)}{[\overline{a^{2n}} - (\overline{a^n})^2]}. \tag{5}$$

Values of τ_n can therefore be estimated from the spectrum of a^n providing adequate low frequency spectral data are available (see Comte-Bellot & Corrsin 1971). The observed spectra, to be presented later, became reasonably flat as $\omega \to 0$ and the limit was evaluated by extrapolating the data to zero frequency. It is assumed that this provides reasonably representative values of the integral scales. The values so obtained for the u signal are $\tau_1 = 8{\cdot}6 \times 10^{-3}$, $\tau_2 = 4{\cdot}9 \times 10^{-3}$, $\tau_3 = 5{\cdot}3 \times 10^{-3}$ and $\tau_4 = 2{\cdot}9 \times 10^{-3}$ s. The integral scales of the powers of $u(t)$ are of the same order of magnitude as that for $u(t)$ itself. This result is not surprising as the velocity signal is reasonably Gaussian (Lumley & Panofsky 1964). Using these estimates, the values of the moments from table 3 and equations (2), one obtains

$$\epsilon^2(\sigma^2) = 1{\cdot}57 \times 10^{-2}/T, \quad \epsilon^2(S\sigma^3) = 8{\cdot}76 \times 10^{1}/T, \quad \epsilon^2(K\sigma^4) = 3{\cdot}86 \times 10^{-2}/T. \tag{6}$$

The predicted integration times to obtain the moments with 5 % accuracy are therefore 6 s for the variance, $3{\cdot}5 \times 10^4$ s for the skewness, and 15 s for the flatness factor. The even-order moments converge quite rapidly relative to the odd-order moments and this was borne out experimentally. The even-order moments to eighth order would converge to within 5 % of their final values within roughly $10^3 \tau_1$. The relatively smaller in magnitude odd-order moments converged very slowly and tended to exhibit a trend behaviour where the values changed a little in the same direction with each additional ensemble for several ensembles, making it difficult to determine when statistical convergence was achieved. Some indication of this behaviour is shown in table 4, which presents moment values obtained with different sampling intervals and for several integration times with fixed sampling frequency. The data were obtained for the $u(t)$ signal at $\eta = -0{\cdot}019$ and the signal was low-pass filtered at twice Kolmogorov's frequency for all runs. The sampling interval is Δt, N is the total number of samples and $T = N\Delta t$ is the total sampling period. The first three rows give the moment estimates for three different sampling intervals for a fixed total sampling

Δt (s)	N (T, min)	$\overline{u^3}/\tilde{u}^3$	$\overline{u^4}/\tilde{u}^4$	$\overline{u^5}/\tilde{u}^5$	$\overline{u^6}/\tilde{u}^6$	$\overline{u^7}/\tilde{u}^7$	$\overline{u^8}/\tilde{u}^8$
$5{\cdot}60 \times 10^{-5}$	$1{\cdot}8 \times 10^6$ (1·7)	−0·072	2·61	−0·40	10·4	−1·81	54·1
$6{\cdot}64 \times 10^{-4}$	$1{\cdot}5 \times 10^5$ (1·7)	−0·010	2·63	+0·01	10·5	+0·69	53·8
$1{\cdot}66 \times 10^{-3}$	$6{\cdot}0 \times 10^4$ (1·7)	−0·022	2·63	−0·06	10·4	−0·27	53·3
$6{\cdot}64 \times 10^{-4}$	$2{\cdot}7 \times 10^6$ (30)	−0·035	2·60	−0·16	10·2	−0·37	52·4
$1{\cdot}663 \times 10^{-3}$	$1{\cdot}08 \times 10^6$ (30)	−0·027	2·60	−0·10	10·3	+0·17	52·6
$1{\cdot}663 \times 10^{-3}$	$3{\cdot}0 \times 10^6$ (83)	−0·035	2·60	−0·16	10·2	−0·27	52·1

TABLE 4

period of 1·7 min. The Kolmogorov time scale τ_K is $1{\cdot}3 \times 10^{-4}$ s, so the sampling intervals covered the range from approximately $\frac{1}{2}\tau_K$ to nearly the integral scale values with no apparent effect on the even moments. The fourth and fifth rows give a comparison between two sampling rates at $T = 30$ min. The last row shows the estimates after $N = 3 \times 10^6$ samples at $T = 83$ min, and (6) predicts the variance to be determined to within $\pm 0{\cdot}2$ %, the skewness to within ± 13 %, and the flatness factor to within $\pm 0{\cdot}3$ %. As the running means of the moments were printed out with the on-line printer after each ensemble was processed, the convergence of the moment estimates was monitored, and the predictions from (6) are consistent with the observations. The sixth- and eighth-order moments were observed to converge to stable estimates to within $\pm 0{\cdot}3$ % while the fifth and seventh moments converged to within ± 15 %. As the sampling interval used has no effect on the final moment estimates, as is expected for stationary random signals, the optimum sampling interval is one that provides adjacent samples that are approximately independent of each other. Tennekes & Lumley (1972) show that this requires the sampling interval to be equal to or greater than twice the integral time scale. The largest Δt used in this test was $1{\cdot}66 \times 10^{-3}$ s, which is less by a factor of four than the integral time scale of the basic signal $u(t)$ and about half that of the $u^4(t)$ signal, so the adjacent samples were not quite independent. In applying (1), it is tacitly assumed that the frequency and amplitude response of the processing circuits is adequate. This can be determined only *a posteriori* by analysis of spectral and moment integrand plots for the signals measured. The spectral plots will be considered subsequently. The distributions of the moment integrands for the $u(t)$ signal are shown in figures 11 and 12. These distributions correspond to the moments presented in the last row of table 4 and first row of table 3 and are the results for $N = 3 \times 10^6$ samples. These figures clearly demonstrate that the dynamic range of the processing circuits ($\pm 5\sigma$ this case) was adequate and the integrand estimates exhibit a high degree of statistical stability.

As pointed out previously, the probability distributions show increasingly non-Gaussian behaviour away from the centre of the flow. Rather large values of

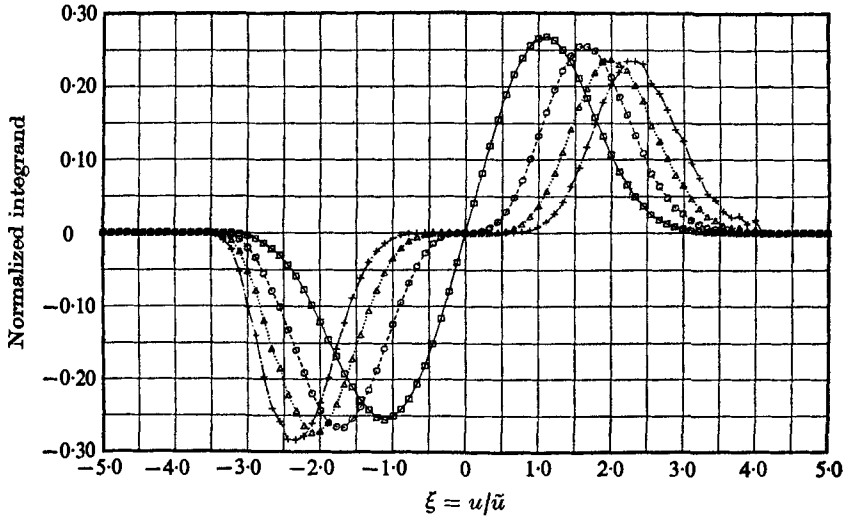

FIGURE 11. Normalized moment integrand distributions for $u(t)$ measured at $\eta = 0{\cdot}019$. □, $\xi p(\xi)$; ○, $0{\cdot}50\ \xi^3 p(\xi)$; △, $0{\cdot}140\ \xi^5 p(\xi)$; +, $0{\cdot}014\ \xi^7 p(\xi)$.

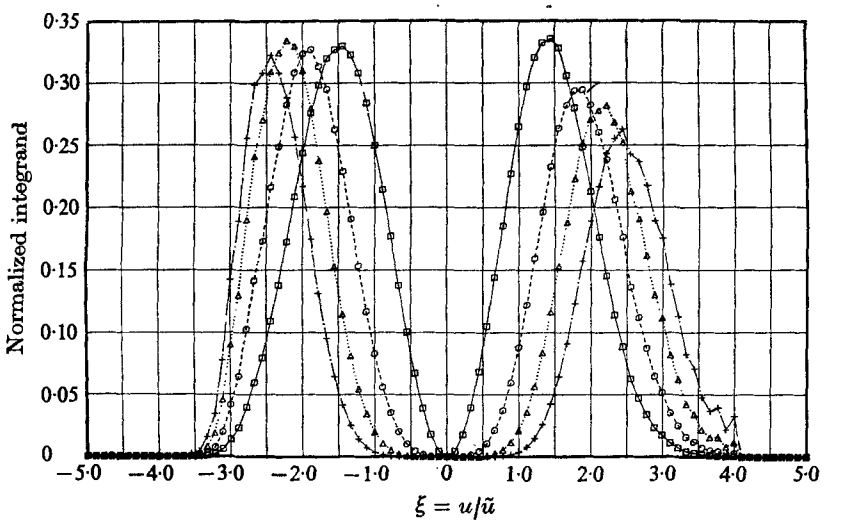

FIGURE 12. Normalized moment integrand distributions for $u(t)$ measured at $\eta = -0{\cdot}019$. □, $\xi^2 p(\xi)$; ○, $0{\cdot}333\ \xi^4 p(\xi)$; △, $0{\cdot}080\ \xi^6 p(\xi)$; +, $0{\cdot}014\ \xi^8 p(\xi)$.

the higher-order moments are therefore encountered and more stringent dynamic-range requirements are imposed on the processing circuits. For comparison, figures 13 and 14 show the moment integrand distributions at $\eta = -0{\cdot}113$ for the $u(t)$ signal, and the moment values are $S = -1{\cdot}45$, $K = 8{\cdot}4$, $M_5 = -33{\cdot}0$, $M_6 = 181$, $M_7 = -984$ and $M_8 = 6 \times 10^3$. The total sampling period is $T = 25$ min and $N = 3 \times 10^6$. The rather large excursions in the distributions at $u/\tilde{u} = -8{\cdot}9$ result from seventeen observations out of the total of 3×10^6, so the statistical stability of this probability density estimate is questionable. The values of the

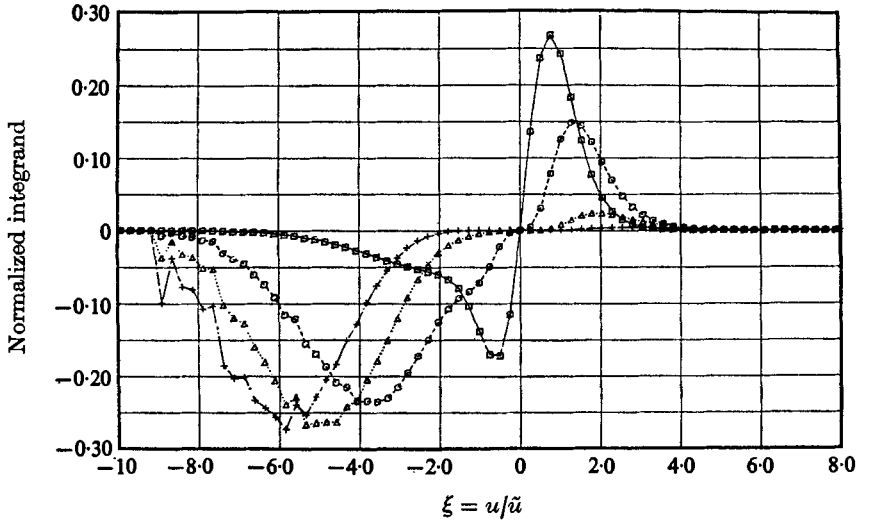

FIGURE 13. Normalized moment integrand distributions for $u(t)$ measured at $\eta = -0{\cdot}113$. □, $\xi p(\xi)$; □, $0{\cdot}50\ \xi^3 p(\xi)$; △, $3 \times 10^{-2}\ \xi^5 p(\xi)$; +, $10^{-3}\ \xi^7 p(\xi)$.

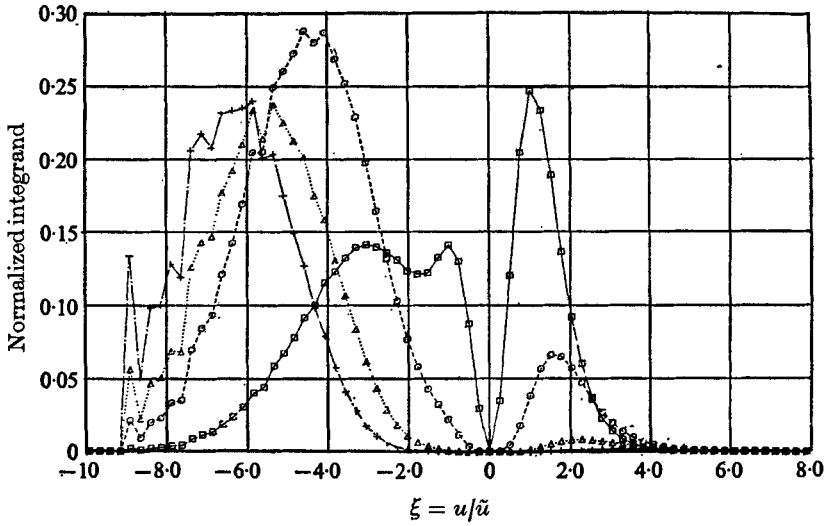

FIGURE 14. Normalized moment integrand distributions for $u(t)$ measured at $\eta = -0{\cdot}113$. □, $\xi^2 p(\xi)$; ○, $0{\cdot}15\ \xi^4 p(\xi)$; △, $5 \times 10^{-3}\ \xi^6 p(\xi)$; +, $1{\cdot}5 \times 10^{-3}\ \xi^8 p(\xi)$.

seventh- and eighth-order moments for larger values of $|\eta|$ than 0·12 should be considered as order-of-magnitude estimates only.

Similar considerations to those described above must be applied to the derivative signals and emphasis will be placed on the statistics of $\partial u/\partial t$ at $\eta = -0{\cdot}019$, which are presented in table 3. Application of (1) to the derivative signal is complicated by the fact that the integral scale of the fundamental signal $\partial u/\partial t$ is zero as the spectrum of the derivative vanishes at the origin $\omega = 0$. The integral scales of powers of the derivative signal are non-zero as their power spectra exhibit maxima at the origin (Lumley 1970; Friehe, Van Atta & Gibson 1971).

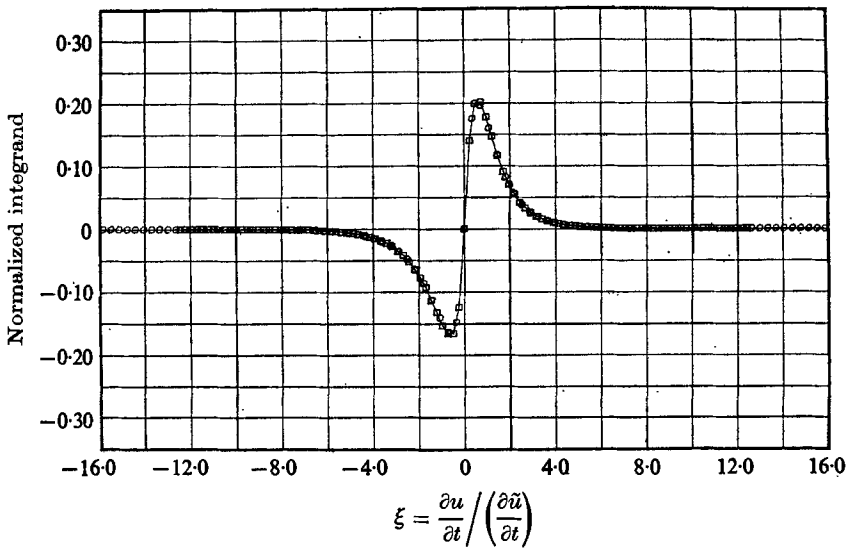

FIGURE 15. Distribution of normalized integrand for first moment of measured probability density of $\partial u/\partial t$. $\eta = -0{\cdot}019$. □, circuit A; ○, circuit B.

Assuming that the integral scale of the $(\partial u/\partial t)^2$ signal is representative of the time interval over which $\partial u/\partial t$ is dependent on itself, we shall use it in estimating the mean-square relative error in both the variance and the flatness factor. Even though the derivative signal is quite non-Gaussian, this substitution should give an order-of-magnitude estimate, which is all we are after in any case. The integral time scales determined from the spectra of $(\partial u/\partial t)^2$ and $(\partial u/\partial t)^3$ give $\tau_2' = 5{\cdot}6 \times 10^{-4}$ s and $\tau_3' = 4 \times 10^{-5}$ s respectively. Tennekes & Wyngaard (1972) considered that a conservative estimate of τ_2' was $10\eta_K/\bar{U}$ on the basis of results obtained by Wyngaard & Pao (1972) and Friehe *et al.* (1971). From the present results, $10\eta_K/\bar{U} = 2{\cdot}5 \times 10^{-4}$ s so it would appear that a better estimate in the present case would be $20\eta_K/\bar{U}$. The moment estimates for $\partial u/\partial t$ shown in table 3 were obtained using a sampling interval of 10^{-3} s, about $2\tau_2'$, for a total sampling period of 46 minutes and $N = 2{\cdot}8 \times 10^6$ samples. The second- and fourth-order moments converged to within $\pm 5\,\%$ of their asymptotic values in about $2 \times 10^5 \tau_2'$, whereas the third, fifth and sixth moments required roughly $3 \times 10^6 \tau_2'$. The seventh moment did not settle down to within a $\pm 5\,\%$ band over the entire run, but appeared to reach a $\pm 10\,\%$ convergence in about $5 \times 10^6 \tau_2$. It is difficult to assign any level of convergence to the eighth moment as it exhibited a trend behaviour and could vary by as much as a factor of 2 during such trends. Application of (2) for the total sampling period indicates that the variance of $\partial u/\partial t$ is determined to within $\pm 0{\cdot}2\,\%$, the skewness to within $\pm 0{\cdot}7\,\%$ and the flatness factor to within $\pm 1{\cdot}6\,\%$. Again we shall consider the dynamic-range requirements by presenting the distributions of the moment integrands for $\partial u/\partial t$, shown in figures 15–22. Results from two different runs are shown, as one run was made with each of two different differentiation circuits. The total number of samples processed by circuit A was $2{\cdot}8 \times 10^6$ and the signal-to-noise ratio S/N and the

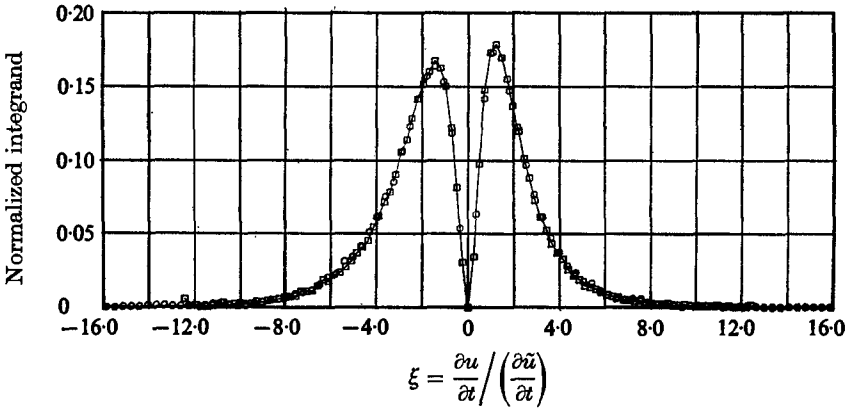

FIGURE 16. Distribution of normalized integrand for second moment of measured probability density of $\partial u/\partial t$. $\eta = -0{\cdot}019$. □, circuit A; ○, circuit B.

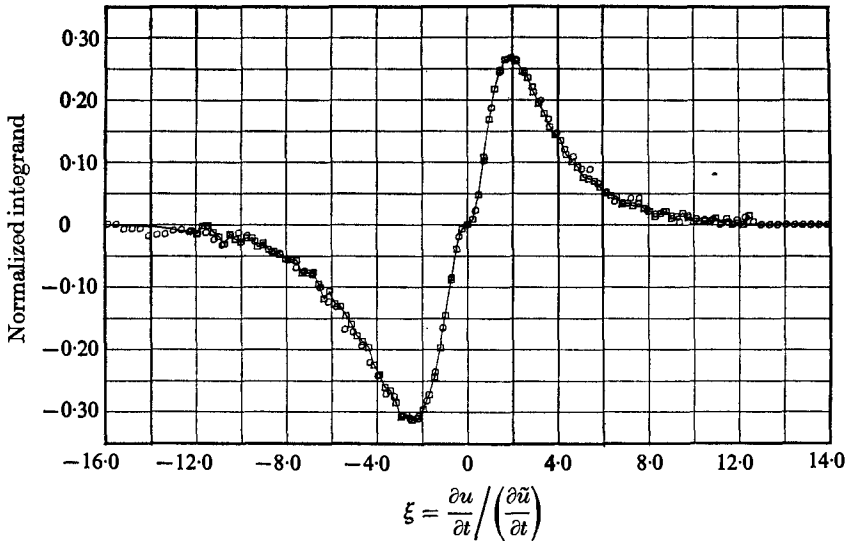

FIGURE 17. Distribution of normalized integrand for third moment of measured probability density of $\partial u/\partial t$. $\eta = -0{\cdot}019$. □, circuit A; ○, circuit B.

dynamic range for the overall circuit were 6 and $\pm 19\sigma$. The reason for using this circuit will be discussed in a subsequent section. For circuit B, the values were $N = 1{\cdot}3 \times 10^6$, $S/N = 20$ and $\pm 20\sigma$; this is the circuit previously described and used in all other derivative measurements. Within the scatter band previously presented, both circuits gave identical results. The integrands of the first, second and third moments converge nicely within the available dynamic range of the circuits and exhibit very little scatter. The scatter in the large amplitude estimates of the higher-order moment integrands, say starting with the fourth, may be due to the lack of statistical stability of the probability density estimates or the occurrence of spurious data samples at large amplitude. The latter problem may be caused by extraneous signal pick-up, large fluctuations in

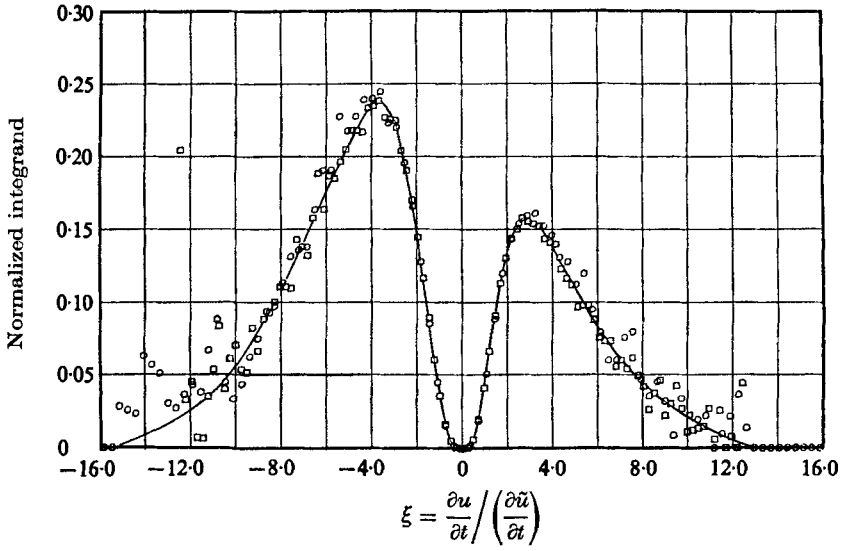

FIGURE 18. Distribution of $0{\cdot}25\ \xi^4 p(\xi)$ measured at $\eta = -0{\cdot}019$. □, circuit A; ○, circuit B.

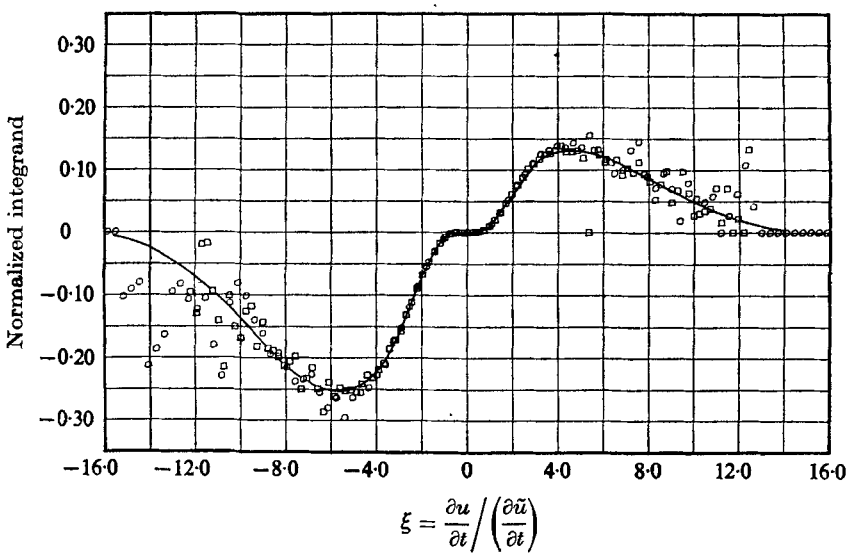

FIGURE 19. Distribution of $6 \times 10^{-2}\ \xi^5 p(\xi)$ measured at $\eta = -0{\cdot}019$. □, circuit A; ○, circuit B.

power-supply voltages, or possibly even some contaminant particle hitting the hot wire. A lack of statistical stability is undoubtedly the most reasonable explanation as typically less than 10 observations out of the total sample populations provide the probability density estimate for amplitudes greater than ± 10. Curves were faired through the integrand distributions up to that for the sixth moment. The fourth moment integrand closes adequately to determine the value of the moment with reasonable accuracy. The integrand for the fifth moment

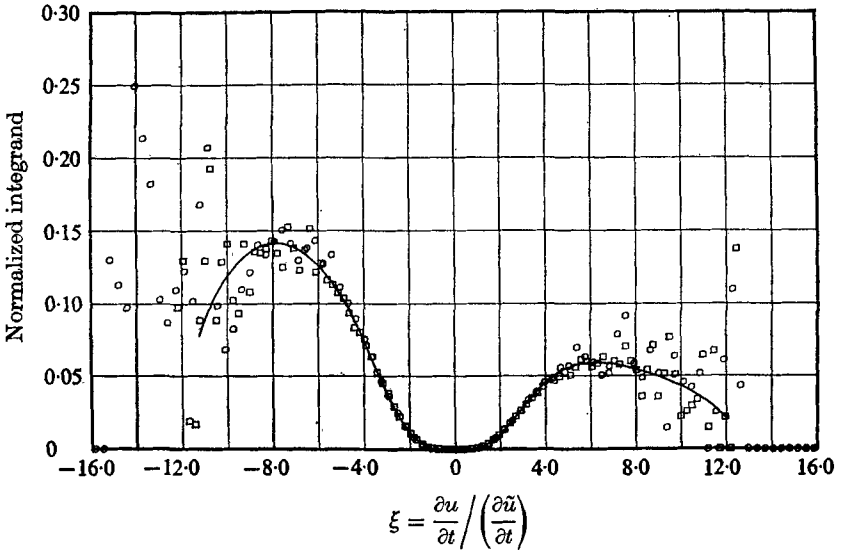

FIGURE 20. Distribution of $5 \times 10^{-3}\, \xi^6 p(\xi)$ measured at $\eta = -0{\cdot}019$. □, circuit A; ○, circuit B.

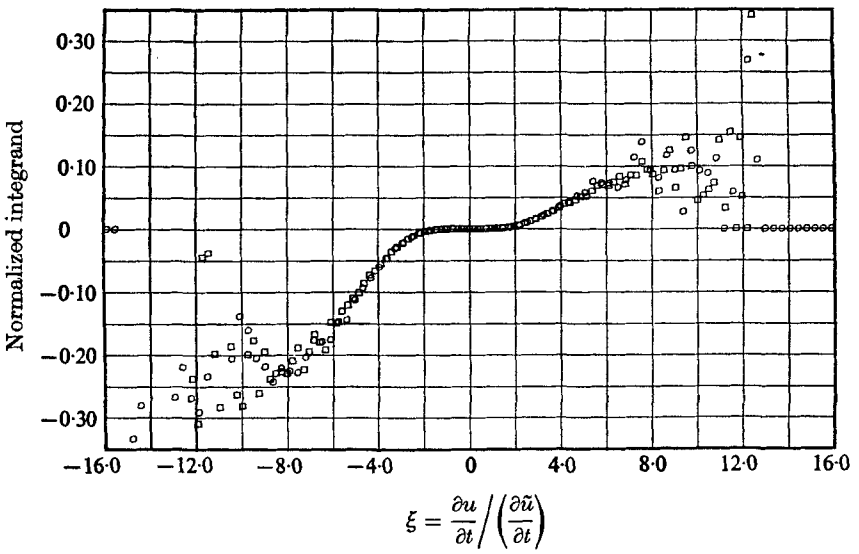

FIGURE 21. Distribution of $10^{-3}\, \xi^7 p(\xi)$ measured at $\eta = -0{\cdot}019$. □, circuit A; ○, circuit B.

does not close as nicely and it is difficult to assign any accuracy to the value of this moment as it is equal to the difference in area determined by the fairing procedure. As the principal contribution to the sixth-, seventh- and eighth-order moments occur at large amplitude values where the scatter makes it difficult to fair in the moment integrand, we can assign only an order-of-magnitude accuracy to the values of these moments. Evaluation of the higher-order moments away from the centre of the flow is even more difficult as their magnitude becomes

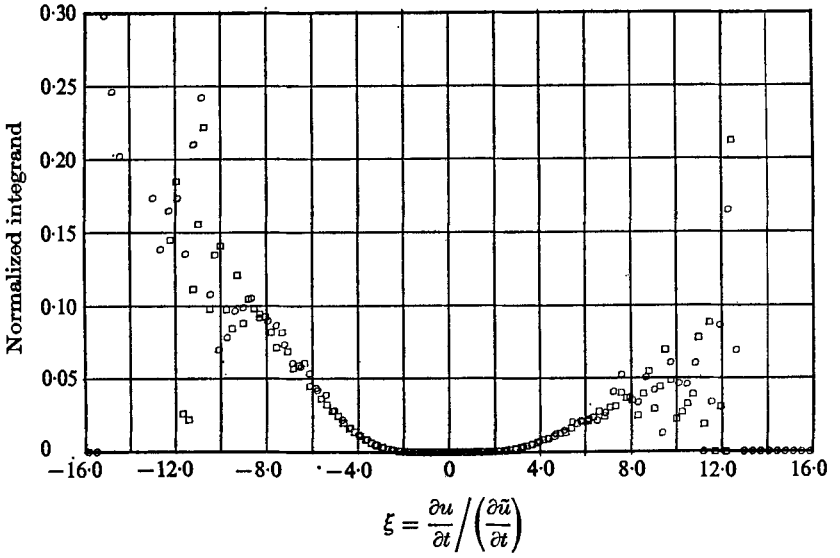

FIGURE 22. Distribution of $5 \times 10^{-5}\ \xi^8 p(\xi)$ measured at $\eta = -0{\cdot}019$. □, circuit A; ○, circuit B.

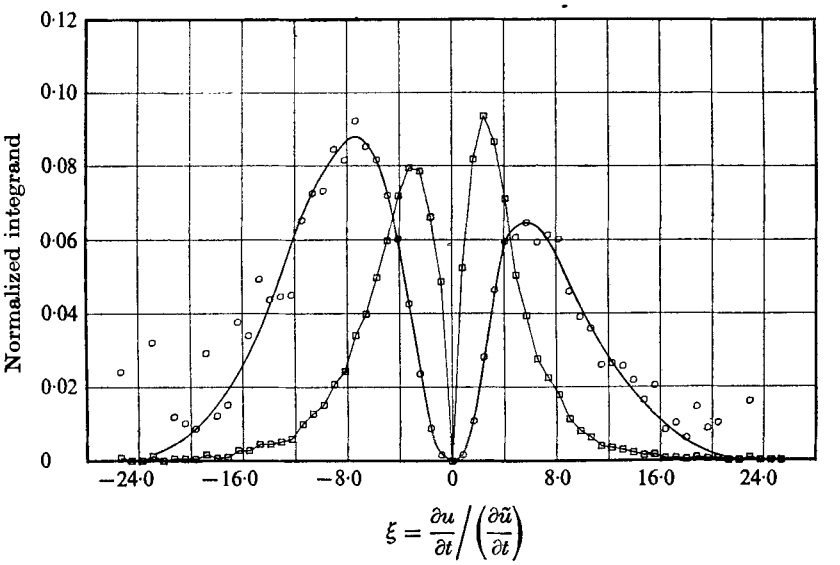

FIGURE 23. Normalized moment integrand distributions for $\partial u/\partial t$ measured at $\eta = -0{\cdot}113$. □, $\xi^2 p(\xi)$; ○, $5 \times 10^2\ \xi^4 p(\xi)$.

large, thereby imposing more stringent dynamic-range and integration time requirements. Figures 23 and 24 show the second, third, fourth and fifth moment integrand distributions for $\eta = -0{\cdot}113$, where the values of the moments are $S = -0{\cdot}66$, $K = 33$, $M_5 = -98$, $M_6 \approx 4 \times 10^3$, $M_7 \approx -2 \times 10^4$ and $M_8 \approx 1 \times 10^6$, the last three values being strictly order-of-magnitude estimates. The spike-like peaks near zero amplitude occurring in the integrand of the first moment were missed because of the rather coarse window width ($\Delta\xi = 0{\cdot}818$) used and thus

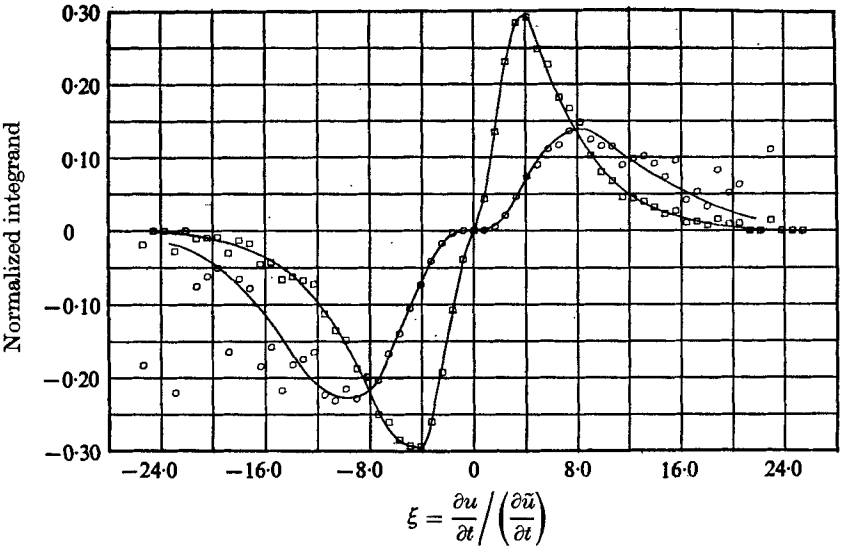

FIGURE 24. Normalized moment integrand distributions for $\partial u/\partial t$ measured at $\eta = -0{\cdot}113$. □, $\xi^3 p(\xi)$; ○, $1{\cdot}5 \times 10^{-2}\, \xi^5 p(\xi)$.

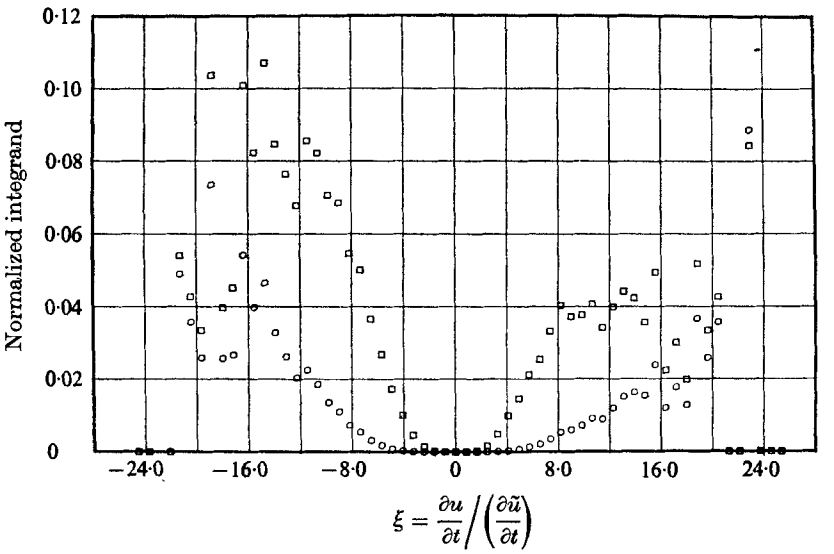

FIGURE 25. Normalized moment integrand distributions for $\partial u/\partial t$ measured at $\eta = -0{\cdot}113$. □, $5 \times 10^{-4}\, \xi^6 p(\xi)$; ○, $10^{-6}\, \xi^8 p(\xi)$.

this integrand is not shown. The signal-to-noise ratio and dynamic range of the processing circuit were 8·3 and $\pm 27\sigma$, respectively. The sampling interval used was $1{\cdot}66 \times 10^{-3}$ s for $N = 1{\cdot}05 \times 10^6$ total samples and a total period of $T = 29$ min. The third and fourth moment integrands require nearly a $\pm 22\sigma$ dynamic range to decrease adequately to a level which allows reasonable determination of the corresponding moment. Thus, as the value of the kurtosis can become quite large in the intermittent region of laboratory turbulent flows, considerable care in the

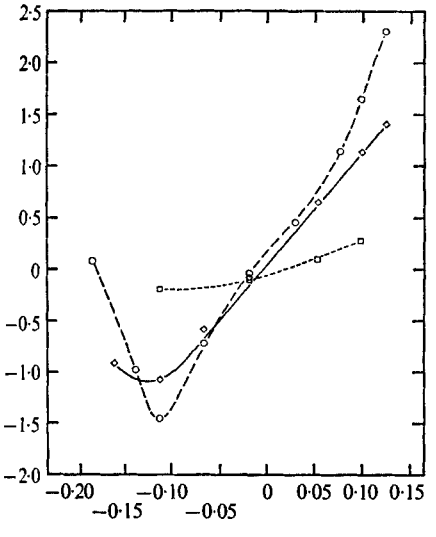

FIGURE 26

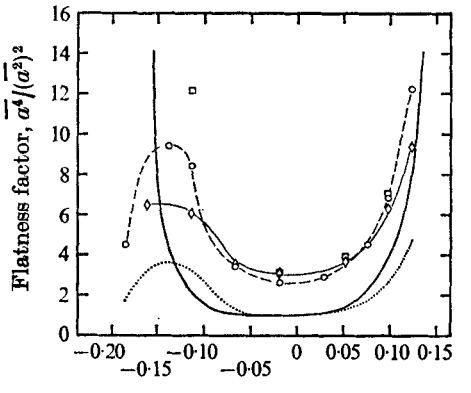

FIGURE 27

FIGURE 26. The distributions of skewness factors. ○, u; ◇, v; □, w.

FIGURE 27. The distribution of flatness factors. ○, u; ◇, v; □, w; ——, $(\gamma_{max}/\gamma)_{meas}$; – – –, $(\gamma_{max}/\gamma)_{F.F.}$.

processing of such signals is required, as in the case of fully turbulent, high Reynolds number atmospheric flow (Tennekes & Wyngaard 1972). The scatter in the integrand estimates for $|\xi| > 20$ can undoubtedly be explained by the lack of statistical stability of the probability density estimate as typically each estimate consisted of only one or two observations out of the $N = 1{\cdot}05 \times 10^6$ samples. The data are barely adequate to describe the fifth moment integrand and again it is difficult to estimate the numerical accuracy estimate of this odd-order moment. Figure 25 shows the sixth- and eighth-order integrands. On the basis of the above results for the velocity-derivative signals, we decided to present the distributions of the moments up to fifth order of the derivative signals across the flow field, with the latter values considered as order-of-magnitude estimates only.

The distributions of the higher-order moments of u, v, and w to seventh order across the flow are shown in figures 26–30. The skewness and flatness-factor distributions agree quite well with the results of W & F, especially for the u-component fluctuations. A comparison of W & F's intermittency results with that computed from the flatness factor is also shown in figure 27.

The skewness of the $\partial u/\partial t$ signal shown in figure 31 differs from the results of W & F on the high velocity side of the flow. The present data indicate a positive skewness increasing in magnitude while the W & F data show a negative skewness increasing in magnitude as the inner edge of the flow is approached. Also shown in figure 31 is the distribution of the fifth moment of the derivative signal while that for the fourth moment is shown in figure 32.

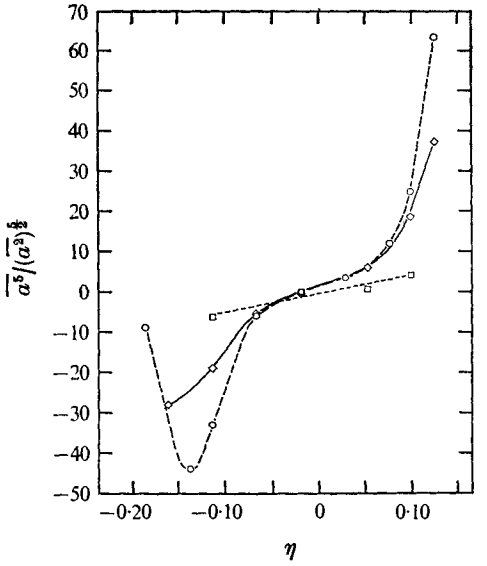

FIGURE 28

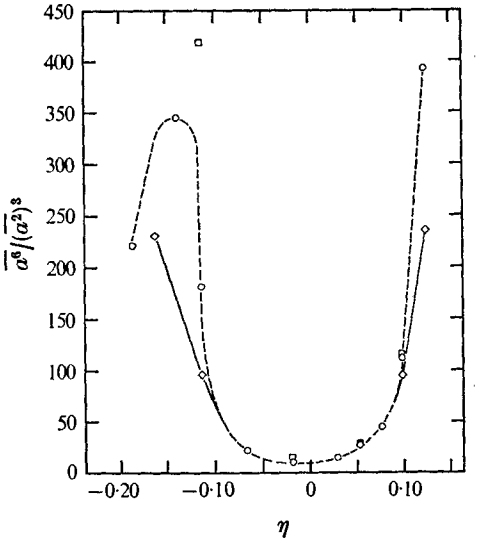

FIGURE 29

FIGURE 28. The distribution of fifth moments. ○, u; ◇, v; □, w.

FIGURE 29. The distribution of sixth moments. ○, u; ◇, v; □, w.

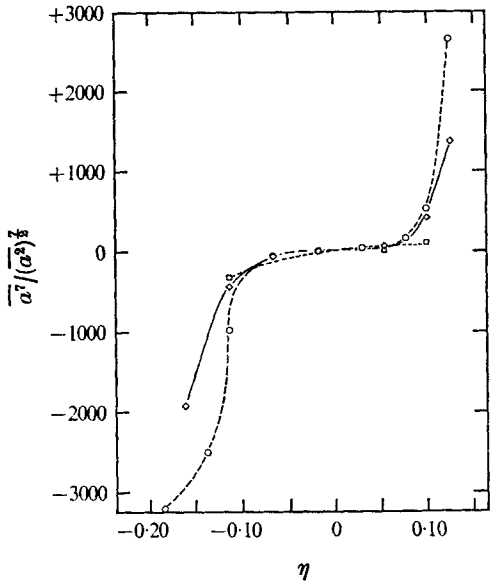

FIGURE 30. Seventh moment distributions. ○, u; ◇, v; □, w.

3.3. *One-dimensional energy spectra and local isotropy*

The one-dimensional energy spectra $F_1(k_1)$, $F_2(k_1)$ and $F_3(k_1)$, whose integrals are $\overline{u^2}$, $\overline{v^2}$ and $\overline{w^2}$, are presented in figure 33 for $\eta = -0{\cdot}019$. Taylor's approximation in the form $k_1 = 2\pi f/\overline{U}$ was used to transform frequency f to wavenumber k_1, the x component. The magnitude of $k_K = \eta_K^{-1}$ is shown, where $\eta_K = (\nu^3/\epsilon)^{\frac{1}{4}}$, the

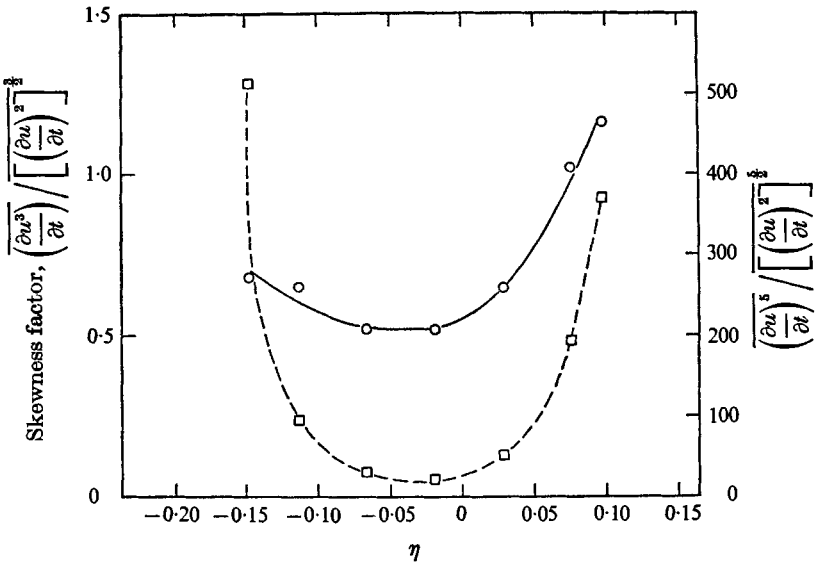

FIGURE 31. The distribution of the skewness and fifth moment of the derivative signal.

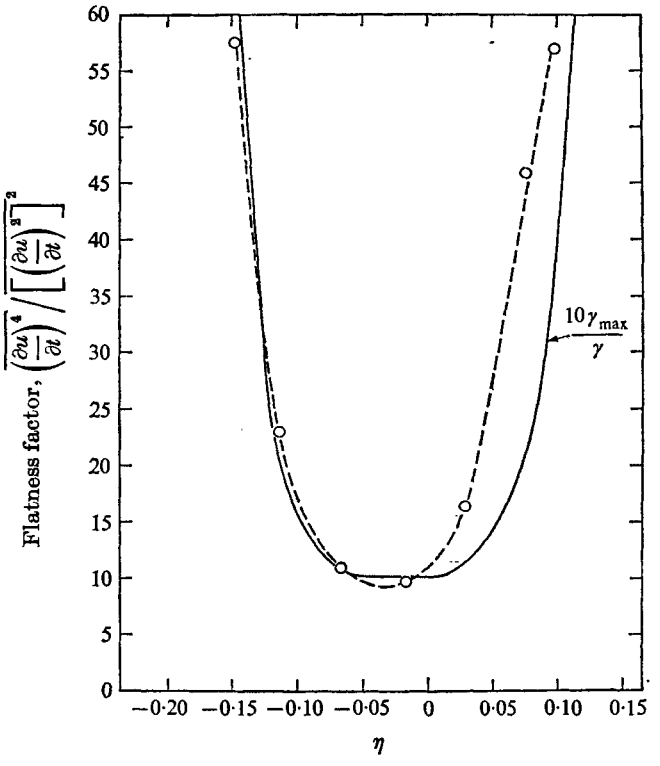

FIGURE 32. The distributions of the flatness factor of the derivative signal.

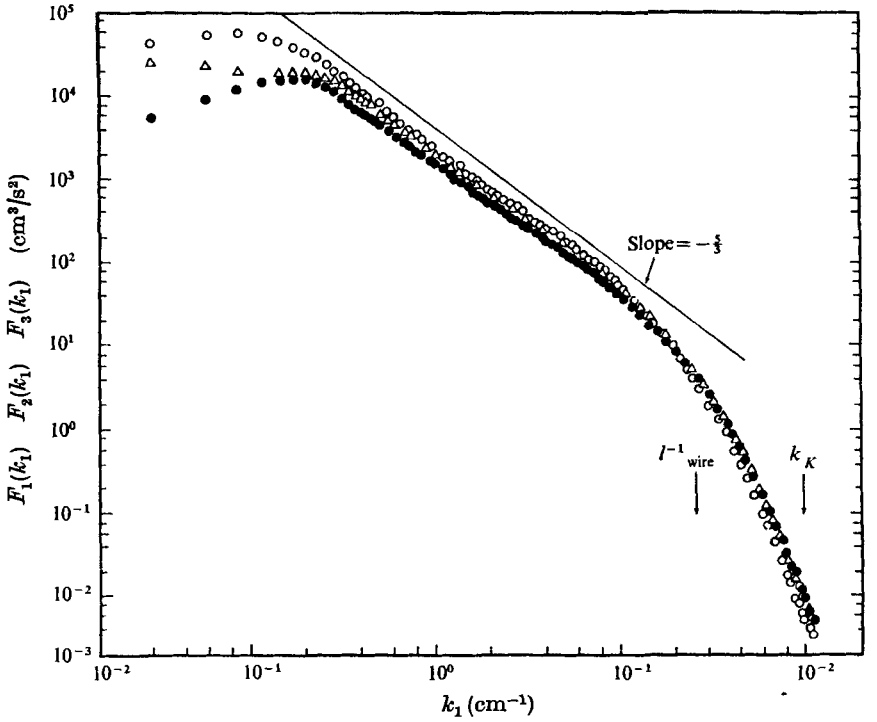

FIGURE 33. One-dimensional energy spectra measured at $\eta = -0{\cdot}019$. ○, $F_1(k_1)$; ●, $F_2(k_1)$; △, $F_3(k_1)$.

Kolmogorov length scale. The value of the dissipation rate ϵ was estimated from $\overline{(\partial u/\partial t)^2}$ using Taylor's hypothesis and assuming local isotropy in the form $\epsilon = 15\nu\overline{(\partial u/\partial x)^2}$. The spectral equivalent of the hot-wire sensing-element length l_w is also indicated. The u spectrum was obtained from a single wire normal to the flow, while the v and w spectra were obtained from X-wires. For both single and X-wires, $\eta/l_w = 0{\cdot}26$. Wyngaard (1969) has shown that, if a 90% response to $\overline{(\partial u/\partial x)^2}$ is required, then wires no longer than 4η can be used in the measurement. The estimate of $\overline{(\partial u/\partial x)^2}$ is therefore essentially unaffected by wire-length attenuation, whereas the actual estimates of the spectral values at wavenumbers greater than l_w^{-1} become increasingly attenuated until at $k_1 = k_K$ the predicted attenuation is about 30% (Wyngaard 1968). For wavenumbers less than l_w^{-1}, the attenuation can be neglected and the measured spectral values should be good estimates of the true spectra. No wire-length corrections were applied to the data.

On the log–log plot shown in figure 33, there appears to be over a decade and a half of a spectral inertial subrange with a $-\frac{5}{3}$ power law behaviour, although the turbulence Reynolds number is only 330. The turbulence Reynolds number R_λ is defined as

$$R_\lambda = \tilde{u}\lambda_g/\nu, \tag{7}$$

where λ_g is the lateral Taylor microscale and was estimated from ϵ and $\tilde{u}$ according to (Hinze 1959)

$$\epsilon = 15\overline{\nu u^2}/\lambda_g^2. \tag{8}$$

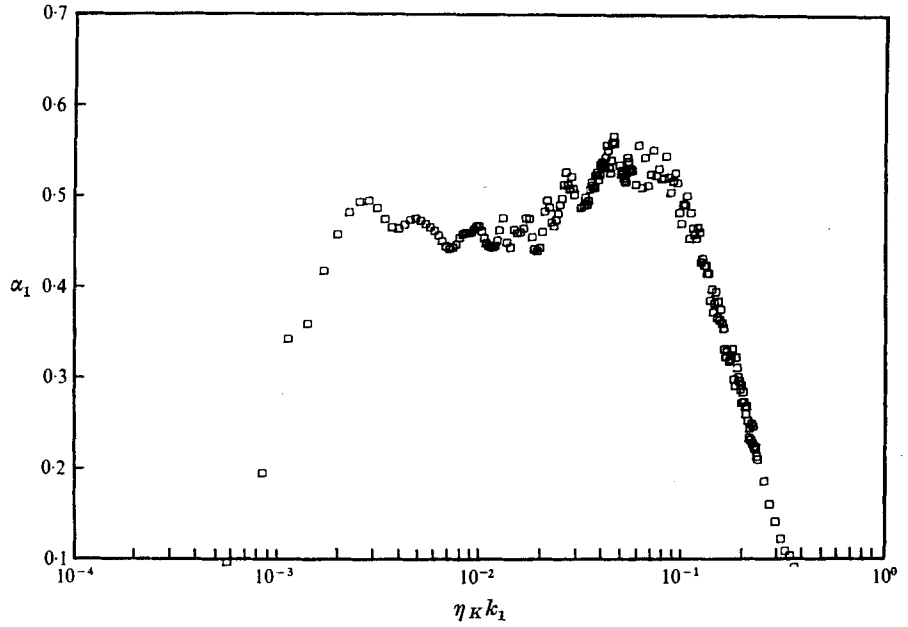

FIGURE 34. One-dimensional Kolmogorov inertial-subrange constant *vs.* normalized wavenumber.

The value of R_λ is probably not large enough to expect local isotropy in the inertial range of the spectrum as the dissipative region may not be separated sufficiently from the production region (Corrsin 1957). The form of the $F_1(k_1)$ spectrum in the wavenumber region of the apparent inertial subrange can be examined more closely by plotting the function $k_1^{\frac{5}{3}} F_1(k_1)$ *vs.* k_1 on a linear–log plot. An equivalent plot is that of α_1 *vs.* $\eta_K k_1$, where α_1 is the one-dimensional Kolmogorov inertial-subrange constant defined by

$$\Phi_1(\eta_K k_1) = \alpha_1 (\eta_K k_1)^{-\frac{5}{3}}, \tag{9}$$

where $\Phi_1(\eta_K k_1) = F_1(k_1)(\nu^{\frac{5}{4}}\epsilon^{\frac{1}{4}})$ is the Kolmogorov normalized spectral function. Such a plot is shown in figure 34. Out of the 4096 total spectral estimates available, the computer was programmed to print out 250 to give a reasonably uniform coverage of the entire frequency/wavenumber range. The scatter band for the spectral points was estimated to be $\pm 5\%$ from intermediate computer print-outs. Within this scatter band, one might conjecture that an inertial subrange exists in the range $3{\cdot}5 \times 10^{-3} < \eta_K k_1 \leqslant 2 \times 10^{-2}$ with a universal constant of $\alpha_1 = 0{\cdot}46$. However a necessary requirement for local isotropy is that the inertial spectral region be at wavenumbers much larger than those at which turbulent energy production occurs, and the latter were shown by Corrsin (1958) to be

$$k_P \approx \tilde{v}^{-1} \partial \overline{u} / \partial y. \tag{10}$$

For $\eta = -0{\cdot}019$, $\eta_K k_P \approx 8 \times 10^{-3}$. Therefore, as most of the production occurs in the wavenumber region of interest, the inertial-subrange conjecture must be rejected. Further, the $F_2(k_1)$ and $F_3(k_1)$ spectra are less than $F_1(k_1)$ through this

wavenumber region, which contradicts the locally isotropic inertial-subrange relation $F_2(k_1) = F_3(k_1) = \frac{4}{3}F_1(k_1)$. A disturbing feature of the α_1 plot is the evident increase in the value of α_1 with increasing $\eta_K k_1$ in the wavenumber region $2 \times 10^{-2} < \eta_K k_1 < 6 \times 10^{-2}$. This would indicate a decrease in the slope of the spectrum between the apparent inertial subrange and the viscous subrange and thus provides further evidence against the existence of a locally isotropic inertial subrange in the present spectra. We must conclude that the apparent existence of a Kolmogorov $-\frac{5}{3}$ law in u-component spectra, even with proper universal constant magnitude, is a relatively insensitive indicator of local isotropy (Bradshaw 1967; Champagne, Harris & Corrsin 1970). Dissipative local isotropy requires at least $k_K \gg k_P$ and for $\eta = -0{\cdot}019$, $k_K/k_P \approx 125$, which would seem sufficient. As the wire-length attenuation effects come into play over much of the dissipative region, no attempt was made to determine whether the isotropic relation

$$F_2(k_1) = F_3(k_1) = \tfrac{1}{2}[F_1(k_1) - k_1(\partial F_1/\partial k_1)] \tag{11}$$

was valid in this wavenumber region. However, the isotropic form relating the streamwise derivatives,

$$\overline{(\partial u/\partial x)^2} = \tfrac{1}{2}\overline{(\partial v/\partial x)^2}, \tag{12}$$

was found not to hold as the ratio of measured squared derivatives was not $\frac{1}{2}$, but 0·87.

The second moment of the Kolmogorov normalized spectrum $\Phi_1(\eta k_1)$, which is constrained to have the isotropic property

$$\frac{1}{15} = \int_0^\infty (\eta_K k_1)^2 \, \Phi_1(\eta_K k_1) \, d(\eta_K k_1), \tag{13}$$

is shown in figure 35. This spectrum has a peak value of approximately 0·23 at $\eta_K k_1 \approx 0{\cdot}10$, which agrees well with other laboratory results for R_λ in the range 100–300 (Wyngaard & Pao 1972). No corrections to the spectra for effects caused by deviation from Taylor's hypothesis (Lumley 1965) were carried out. The fourth moment is shown in figure 36. Also shown in figures 35 and 36 are the second and fourth moments obtained with a hot wire whose sensing-element length l_w is equal to 12η. The latter spectrum was normalized with the ϵ value obtained with the smaller wire ($l_w \approx 4\eta$) to show the attenuation properly. These data were obtained to confirm the attenuation calculations of Wyngaard (1968) and good agreement was obtained. These results, however, provide only a check on the *relative* attenuation between two wires whose lengths are both greater than Kolmogorov's microscale, rather than a check on the absolute attenuation, which requires that one of the spectra be measured with a hot wire whose length is equal to or less than η_K.

Finally, the spectra of the streamwise velocity fluctuations at the flow centre and the two half-intensity points are shown in figure 37. The spectra are plotted in the form $F_1(f)$ normalized by the local variance of the fluctuations *vs.* frequency to determine whether the low frequency regions exhibit rather narrow spectral peaks as observed by Spencer (1970) in his large shear case, $r = 0{\cdot}6$. He measured

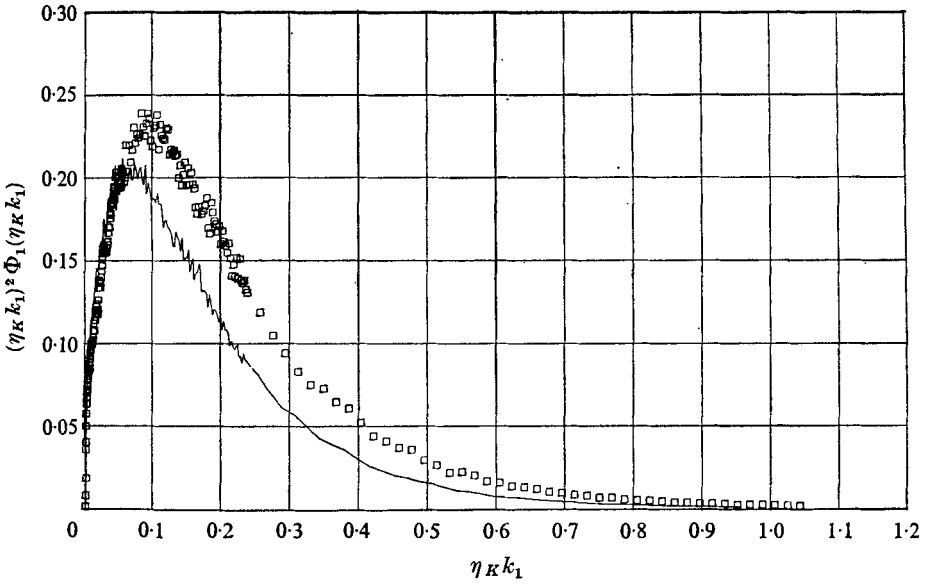

FIGURE 35. Second moment of the measured spectra.
$\eta = -0{\cdot}019$. □, $l_w/\eta = 4$; ——, $l_w/\eta = 12$.

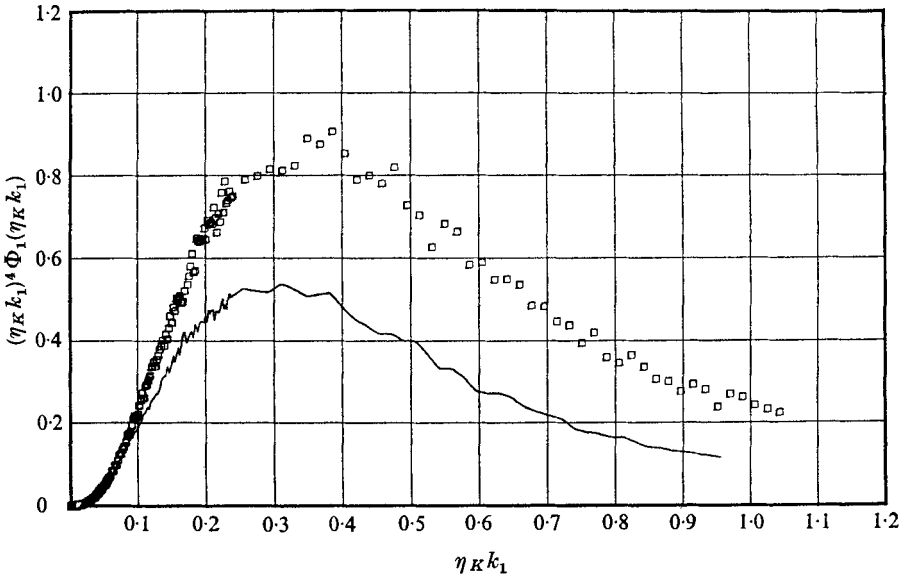

FIGURE 36. Fourth moment of the measured spectra.
$\eta = -0{\cdot}019$. □, $l_w/\eta = 4$; ——, $l_w/\eta = 12$.

u-component spectra at the flow centre and at the position where $\gamma \approx 0{\cdot}4$ on each side of the mixing layer. The latter two spectra contained narrow peaks at nearly the same frequency, while for the centre of the flow a rather weak peak at a lower frequency was observed. Similar behaviour is not evident in the present flow, as figure 37 shows.

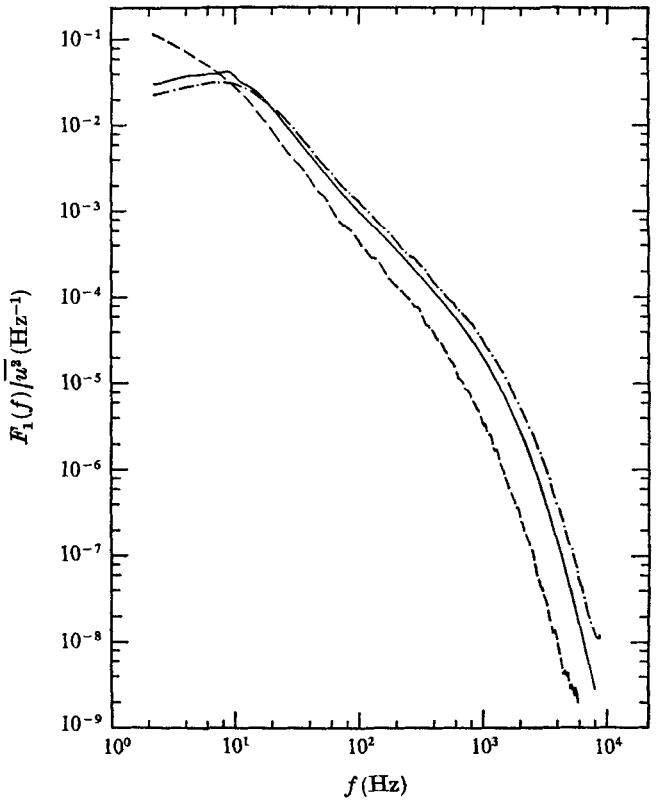

FIGURE 37. One-dimensional energy spectra measured at three transverse positions. ——, $M-1$, $\eta = -0{\cdot}019$; – – –, $M-2$, $\eta = +0{\cdot}097$; —·—, $M-3$, $\eta = -0{\cdot}113$.

3.4. *Higher-order spectra*

The first or variance spectrum and the higher-order spectra of the longitudinal velocity fluctuations are defined as

$$\overline{(u^n - (\overline{u^n}))^2} = \overline{u^{2n}} - (\overline{u^n})^2 = \int_0^\infty {}_nF_1(k_1)\,dk_1, \tag{14}$$

which is similar to the definition presented in §3.2 with application of Taylor's hypothesis to convert frequency to wavenumber. According to the original Kolmogorov theory (1941) the first-order spectrum should take the universal form

$$\Phi_1(\eta_K k_1) = F_1(k_1)/(\nu^{\frac{5}{4}}\epsilon^{\frac{1}{4}}) \tag{15}$$

when normalized by ϵ and ν (for sufficiently large R_λ). Let us consider the case $n = 2$:

$$\overline{u^4} - (\overline{u^2})^2 = \int_0^\infty {}_2F_1(k_1)\,dk_1. \tag{16}$$

If one assumes that Kolmogorov's universal equilibrium theory applies to the statistic ${}_2F_1(k_1)$, then the motion in the equilibrium range of wavenumbers is uniquely determined by ϵ and ν and the second-order spectrum takes the universal form

$${}_2\Phi_1(\eta_K k_1) = {}_2F_1(k_1)/(\nu^{\frac{7}{4}}\epsilon^{\frac{3}{4}}). \tag{17}$$

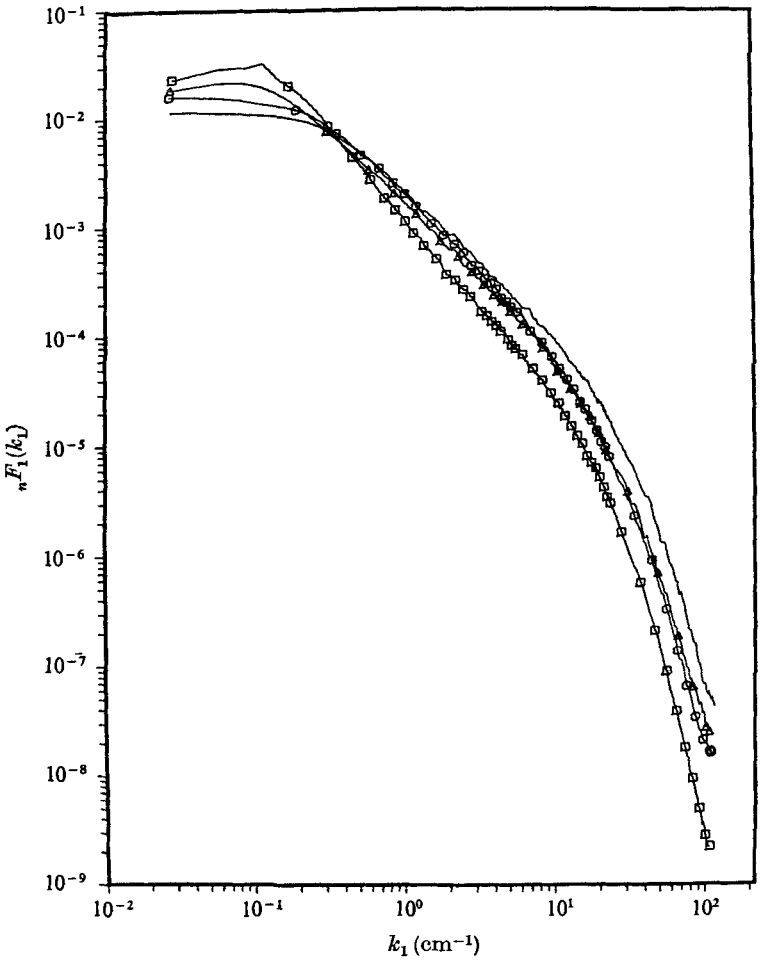

FIGURE 38. Higher-order spectra measured at $\eta = -0{\cdot}019$.
□, $n = 1$; ○, $n = 2$; △, $n = 3$; ——, $n = 4$.

If one goes one step further and assumes that equivalent inertial subranges exist for these higher-order spectra then it can be shown that

$$ {}_2F_1(k_1) \sim k_1^{-\frac{7}{3}}, \quad {}_3F_1(k_1) \sim k_1^{-3}, \quad {}_4F_1(k_1) \sim k_1^{-\frac{11}{3}}, \tag{18} $$

again for sufficiently large R_λ. Figure 38 shows ${}_nF_1(k_1)$ normalized by $\overline{u^{2n}} - (\overline{u^n})^2$ *vs.* wavenumber for $n = 1, 2, 3$ and 4. Although we have shown that an inertial subrange does not exist for the first-order spectra in this flow, one might at least expect qualitative agreement with the spectral forms, but this is not the case. The observed spectral behaviour indicates that the spectra get less steep with increasing order in the wavenumber range where the first-order spectrum approximately follows the $-\frac{5}{3}$ law. It can be shown that for Gaussian noise with a Gaussian autocorrelation function the second-order spectrum is less steep than the first-order spectrum (Corrsin, private communication).

The authors are indebted to Dr J. Lumley for pointing out that if one evaluates

$$\partial^4\{\overline{(u^2(t)-\overline{u^2})\,(u^2(t+\tau)-\overline{u^2})}\}/\partial\tau^4,$$

terms such as $\overline{(\partial u(t)/\partial\tau)^2\,(\partial u(t+\tau)/\partial\tau)^2}$ are obtained which contribute to the spectrum of the dissipation fluctuations. This implies that the higher-wavenumber components of these higher-order spectra must be influenced by the same (fine-scale) intermittency or variability as affects the dissipation fluctuation spectra, and hence cannot follow Kolmogorov scaling.

Yaglom (1966), using the assumptions in Kolmogorov's (1962) refined hypothesis, predicted that the one-dimensional spectrum of the dissipation fluctuations should be of the form

$$E_{\epsilon\epsilon} \sim k_1^{-1+\mu}, \tag{19}$$

where μ is a universal constant. This constant appears in Kolmogorov's formulation for the variance of the logarithm of the viscous dissipation rate ϵ_r averaged over a volume of dimension r^3 as a function of r, given by

$$\sigma^2_{\ln \epsilon_r} = A(x,t) + \mu \ln (L_0/r) \quad (L_0 \gg r \gg \eta), \tag{20}$$

where L_0 is the energy scale of the turbulence and A is a function of the large-scale features of the flow field. As at present no technique is available for measuring dissipation fluctuations, the instantaneous rate of dissipation is assumed to be proportional to $(\partial u/\partial x)^2$, and therefore the spectrum of $(\partial u/\partial x)^2$ is assumed proportional to $k_1^{-1+\mu}$. The problem of representing the instantaneous dissipation rate by $(\partial u/\partial x)^2$ is discussed by Gibson & Masiello (1972) and values of μ obtained in this way are reviewed by Gibson *et al.* (1970). The squared-first-derivative spectra for the u and v signals at $\eta = -0{\cdot}019$ are shown in figure 39. The spectra exhibit approximate power-law behaviour as shown for wavenumbers less than that corresponding to the peak in the dissipation spectrum, i.e. 10 cm^{-1}, and greater than 0·01 cm^{-1}. This is the same wavenumber range as that in which the apparent inertial subrange in the $F_1(k_1)$ spectrum exists. The lines representing the power-law fit to the $(\partial u/\partial t)^2$ and $(\partial v/\partial t)^2$ spectra have slopes of $-0{\cdot}57$ and $-0{\cdot}49$, respectively. The lognormal constants are therefore 0·43 and 0·51, respectively, although the Reynolds number of the turbulence may not be sufficiently large to expect the $k_1^{-1+\mu}$ form to apply. In any case, the power-law behaviour should be expected to apply only in the inertial-subrange wavenumber region because of the requirements on r in (20). If one tried to force the power-law fit into the dissipation wavenumber region a smaller slope would result because of the existence of a spectral bump in this wavenumber region. The spectral bump is evident not only in the present data, but also in those of Stewart, Wilson & Burling (1970), Friehe *et al.* (1971) and Wyngaard & Pao (1972). The lognormal constant inferred from the $(\partial v/\partial t)^2$ spectrum is different from that inferred from the $(\partial u/\partial t)^2$ spectrum and, as the present flow is not locally isotropic, it is difficult to speculate which signal is more representative of the dissipation rate. The reason for the difference is as yet unexplained, although possibly the deviations in the response of a single wire caused by large amplitude fluctuations and large fluctuations in convection velocity (Lumley 1965) are different from

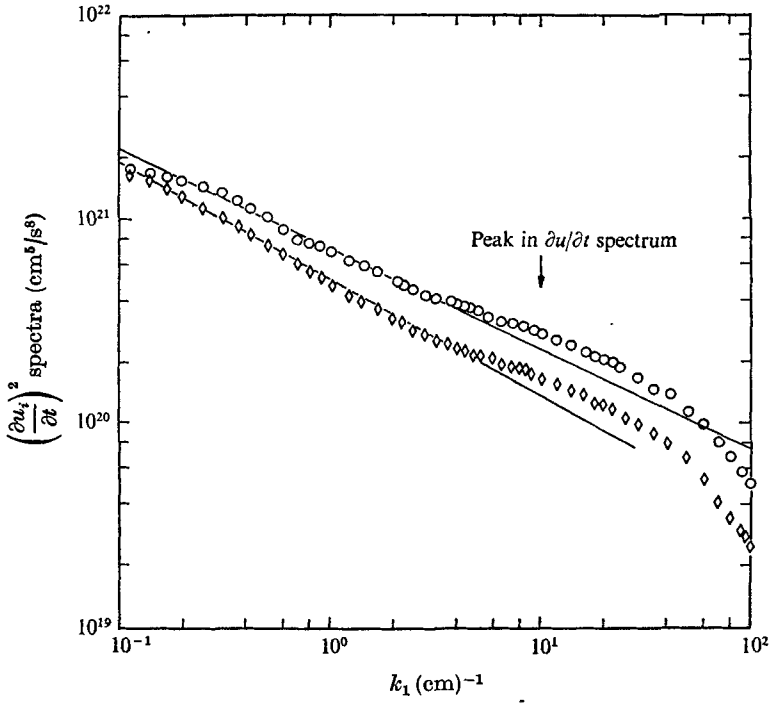

FIGURE 39. Squared-velocity-derivative spectra. $\eta = -0{\cdot}019$. ○, $(\partial v/\partial t)^2$; ◇, $(\partial v/\partial t)^2$.

those for an X-wire, thereby causing different effects on the $(\partial u/\partial t)^2$ and $(\partial v/\partial t)^2$ spectral shapes.

For all the higher-order spectra, the area under each spectral curve provided a value for $\overline{a^{2n}} - (\overline{a^n})^2$, where $a(t)$ is the random signal, which can be compared with the results from the measured moment values. For example, let $n = 2$ and $a = u(t)$; then the area under the second-order spectrum is equal to $\overline{u^4} - (\overline{u^2})^2$, or $(K-1)(\overline{u^2})^2$. As the flatness factor and mean-square value are available from the moment measurements, an independent check on the higher-order moments was possible. Typically, the measured spectral area was within $\pm 5\,\%$ of that predicted from the moment measurements. Also, as the turbulence is stationary, (4) shows that the second-order spectrum can be considered representative of the spectrum of the flatness factor. Similarly, the third- and fourth-order spectra can be considered representative of the sixth- and eighth-order moments, respectively. Thus the higher-order spectra can be used to determine whether the frequency range of the processing circuits was adequate, which was the case here in view of the agreement of the spectral-area calculations.

3.5. *Lognormality of squared-derivative fluctuations*

Gurvich & Yaglom (1967) extended Yaglom's (1966) hypotheses for ϵ_r to include any local non-negative characteristics of the small-scale turbulence, such as the dissipation rate itself or squared derivatives of the velocity fluctuations. Cumulative distribution functions of the logarithm of $(\partial u/\partial t)^2$, $(\partial v/\partial t)^2$ and $(\partial^2 u^2/\partial t^2)$

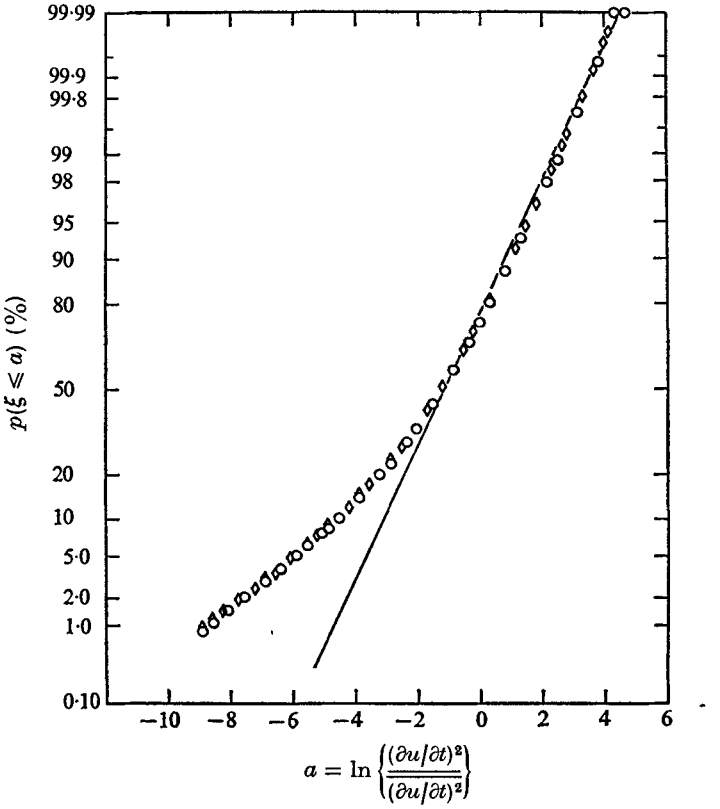

FIGURE 40. Probability distribution of logarithm of squared velocity derivative. $\eta = -0{\cdot}019$. ○, run $LN1$; ◇, run $LN2$.

were determined at the centre of the flow, $\eta = -0{\cdot}019$. The calculation of the distribution functions was performed by first determining the histogram of the squared-derivative samples and then transforming to the histogram of the logarithm via the appropriate identity.

Figure 40 shows a probability plot of the distribution functions of $(\partial u/\partial t)^2$ obtained from two different differentiator circuits. The data labelled run $LN1$ will be considered first. The derivative's square is normalized by the derivative's variance. As pointed out previously, care was taken to avoid phase shifts and amplitude distortion of the derivative signal wave forms. The phase shift of the differentiator circuits was quite linear with frequency over the band of interest and the overall signal-to-noise ratio for the circuit used in run $LN1$ (and $LN3$), circuit B, was 20:1, or 20 dB. The lognormal distribution represented by the solid straight line has a mean and standard deviation (slope) determined from the measured kurtosis of the derivative and in general does not fit the measured distribution function very well. Improvement in the fit through the large amplitude range, excluding the extreme values, is obtained if the line is shifted slightly to the right. Then the line would be tangential to the measured distribution over a limited range and fall below it in the range of the largest amplitude values, in agreement with the results of Gibson & Masiello (1972)

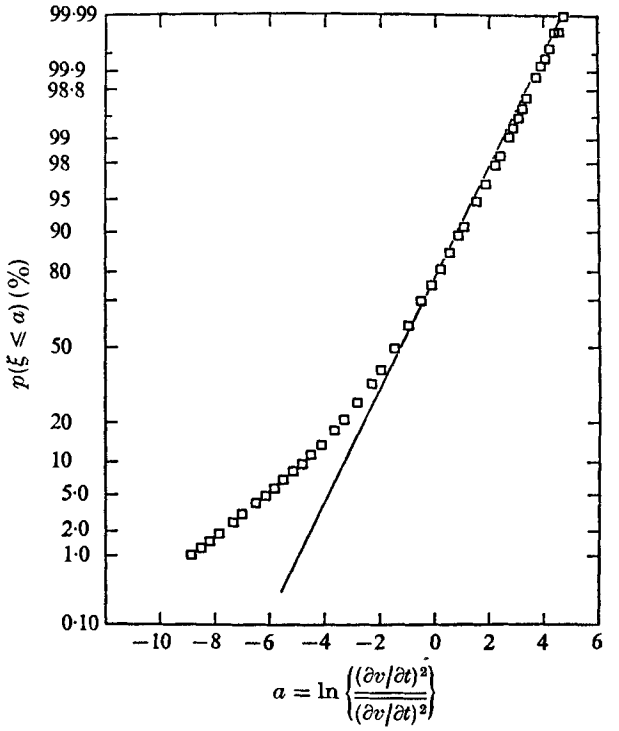

FIGURE 41. Probability distribution of logarithm of squared transverse velocity derivative. $\eta = -0{\cdot}019$.

for their unaveraged data. The deviation at the small amplitude values was attributed to noise by Gibson *et al.* (1970). Stewart *et al.* (1970) and Wyngaard & Tennekes (1970), however, concluded that noise was not the case for the observed characteristic curvature at small values based on computer simulation of lognormal signals containing Gaussian noise. Gibson & Masiello (1972) showed that filtering out noise did not remove the curvature. Further evidence indicating that circuit noise is not the cause of the deviation is provided by the data labelled run $LN2$. These data were obtained with a differentiator circuit, circuit A, similar to the one used in run $LN1$ but with the signal-to-noise ratio lowered to 6. This was achieved by removing one filter and increasing the low-pass setting of the remaining filter from a frequency equivalent to twice Kolmogorov's frequency, $f_K = \bar{U}/2\pi\eta_K$, to $2{\cdot}7f_K$. The measured flatness factors obtained with the two circuits agreed to within 5 % while the skewness factors were within 2 %. As these deviations are within the statistical uncertainty discussed earlier, the result of the filter modification was to add about three times the amount of noise while not distorting the basic derivative signal. Note that there is no significant difference between the two sets of data for the range of small amplitudes where the deviation from the straight line occurs. Gibson & Masiello (1972) indicate that the reason for this deviation could be that $(\partial u/\partial t)^2$ may not be representative of the local value of the dissipation rate ϵ when the value of $(\partial u/\partial t)^2$ is relatively small. In fact they conclude that their

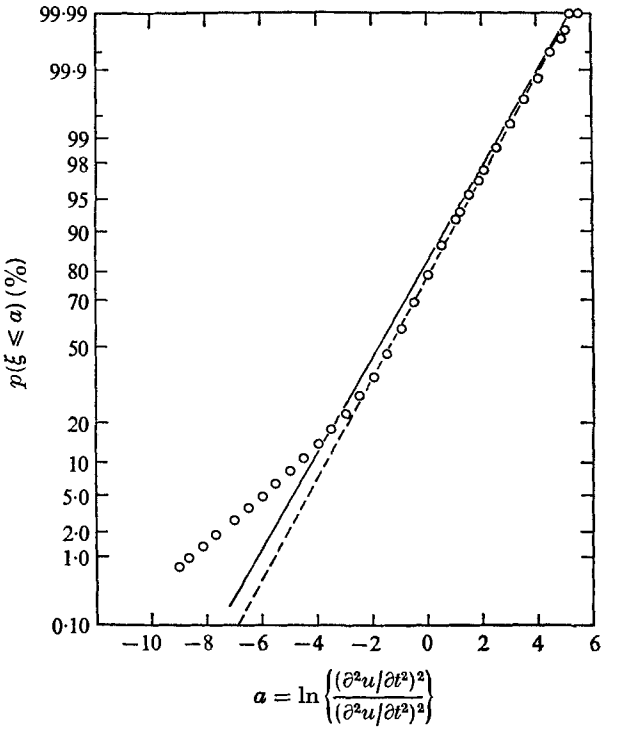

FIGURE 42. Probability distribution of logarithm of squared second derivative of velocity. $\eta = -0{\cdot}019$.

measurements of averaged values of $\epsilon_r \sim (\partial u/\partial t_r)^2$ are consistent with lognormality only under the assumption that the extreme values of the squared derivative are representative of ϵ_r.

The cumulative distribution function for the logarithm of $(\partial v/\partial t)^2$ is shown in figure 41 and the results are quite similar to those for the $\partial u/\partial t$ signal. The lognormality of the second-derivative signal $\partial^2 u/\partial t^2$ is shown in figure 42. The solid straight line was again calculated from the flatness factor of the basic signal. The dashed straight line is faired to the large amplitude data and the fit is quite reasonable down to about 60 %, where the characteristic small amplitude curvature begins. The square of the second derivative shows less departure from lognormality than the square of the first derivative, and this agrees with the results obtained by Kuo (1970) for both low Reynolds number ($R_\lambda = 72$) grid flow and on the axis of an axisymmetric jet with $R_\lambda = 830$.

The authors are indebted to S. Hansen, who developed all the programs for use with the on-line digital data acquisition system, and F. Lange, who provided valuable assistance in constructing and modifying the laboratory equipment. The first author, F. H. C., is grateful to Dr C. H. Gibson, Dr C. A. Friehe, Dr J. C. La Rue and Dr C. Winant for reviewing the manuscript and many helpful suggestions. Also we thank Dr C. H. Gibson for providing funds to support computer preparation of many of the figures using the computer graphics system

AMES PLOT developed by I. Hirschsohn at UCSD. The authors would also like to thank Mrs Jeri Neuberger for typing the manuscript. The research was supported by AFOSR Contract 72-2287, monitored by Capt. W. H. Smith.

REFERENCES

BATT, R. G. 1974 *TRW TR Rep.* no. 18117–6023. (See also *SAMSO TR* no. 74–62.)

BATT, R. G., KUBOTA, T. & LAUFER, J. 1970 *A.I.A.A. Reacting Turbulent Flows Conf., San Diego.*

BLACKMAN, R. B. & TUKEY, J. W. 1958 *The Measurement of Power Spectra.* Dover.

BRADSHAW, P. 1966 *J. Fluid Mech.* **26**, 225.

BRADSHAW, P. 1967 *Nat. Phys. Lab. Aero Rep.* no. 1220.

BROWN, G. & ROSHKO, A. 1971 *AGARD Fluid Dyn. Panel Specialists Meeting on Turb. Shear Flows, London.*

CASTRO, I. P. 1973 Ph.D. thesis, Department of Aeronautics, Imperial College, London.

CHAMPAGNE, F. H., HARRIS, V. G. & CORRSIN, S. 1970 *J. Fluid Mech.* **41**, 81.

CHAMPAGNE, F. H., SLEICHER, C. A. & WEHRMANN, O. 1967 *J. Fluid Mech.* **28**, 153.

COMTE-BELLOT, G. & CORRSIN, S. 1971 *J. Fluid Mech.* **48**, 273.

COOLEY, J. W., LEWIS, P. A. W. & WELCH, P. D. 1967 *IBM Watson Res. Center, Yorktown Heights, New York, Paper,* RC-1743.

CORRSIN, S. 1950 *J. Aero Sci.*. **17**, 396.

CORRSIN, S. 1957 *Proc. 1st Naval Hydro-Symp., Nat. Acad. Sci./Nat. Res. Counc.* publ. 515, p. 373.

CORRSIN, S. 1958 *N.A.C.A. Res. Memo.* RM 58B11.

CROW, S. & CHAMPAGNE, F. H. 1971 *J. Fluid Mech.* **48**, 547.

FRENKIEL, F. N. & KLEBANOFF, P. S. 1971 *J. Fluid Mech.* **48**, 183.

FRIEHE, C. A., VAN ATTA, C. W. & GIBSON, C. H. 1971 *AGARD Conf. Proc.* no. 93, paper 18–1.

GIBSON, C. H. & MASIELLO, P. 1972 *Proc. Symp. on Stratified Models and Turbulence, Lecture Notes in Physics,* vol. 12, p. 426. Springer.

GIBSON, C. H., STEGEN, G. R. & WILLIAMS, R. B. 1970 *J. Fluid Mech.* **41**, 153.

GURVICH, A. S. & YAGLOM, A. M. 1967 *Phys. Fluids Suppl.* **10**, S59.

HINZE, J. O. 1959 *Turbulence.* McGraw-Hill.

KOLMOGOROV, A. N. 1941 *Dokl. Akad. Nauk. SSR* **30**, 301.

KOLMOGOROV, A. N. 1962 *J. Fluid Mech.* **13**, 82.

KUO, A. 1970 Ph.D. thesis, Department of Mechanics, Johns Hopkins University.

KUO, A. & CORRSIN, S. 1972 *J. Fluid Mech.* **56**, 447.

LIEPMAN, H. W. & LAUFER, J. 1947 *N.A.C.A. Tech. Note,* no. 1257.

LUMLEY, J. L. 1965 *Phys. Fluids,* **8**, 1056.

LUMLEY, J. L. 1970 *Stochastic Tools in Turbulence.* Academic.

LUMLEY, J. L. & PANOFSKY, H. 1964 *Structure of Atmospheric Turbulence.* Interscience.

OBOUKHOV, A. M. 1962 *J. Fluid Mech.* **13**, 77.

PAO, Y. H., HANSEN, S. & MACGREGOR, G. 1969 *Boeing Sci. Res. Lab. Doc.* D1-82-0863.

PATEL, R. P. 1973 *A.I.A.A. J.* **11**, 67.

SPENCER, B. W. 1970 Ph.D. thesis, Department of Nuclear Engineering, University of Illinois.

SPENCER, B. W. & JONES, B. G. 1971 *A.I.A.A. Paper,* no. 71–613.

STEWART, R. W., WILSON, J. R. & BURLING, R. W. 1970 *J. Fluid Mech.* **41**, 141.

SUNYACH, M. 1971 Ph.D. thesis, L'Universite' Claude Bernard de Lyon.

TENNEKES, H. & LUMLEY, J. L. 1972 *A First Course in Turbulence.* M.I.T. Press.

TENNEKES, H. & WYNGAARD, J. C. 1972 *J. Fluid Mech.* **55**, 93.

VAN ATTA, C. W. & CHEN, W. Y. 1970 *J. Fluid Mech.* **44**, 145.

WEILER, H. S. & BURLING, R. W. 1967 *J. Atmos. Sci.* **24**, 653.

WINANT, C. 1972 Ph.D. thesis, Department of Aerospace Engineering, University of Southern California.

WYGNANSKI, I. J. & FIEDLER, H. 1970 *J. Fluid Mech.* **41**, 327.

WYGNANSKI, I. J. & GARTSHORE, I. S. 1963 *McGill University, Mech. Engng Tech. Note*, no. 63–7.

WYNGAARD, J. C. 1968 *J. Sci. Instrum.* **1** (2), 1105.

WYNGAARD, J. C. 1969 *J. Sci. Instrum.* **2** (2), 983.

WYNGAARD, J. C. & PAO, Y. H. 1972 In *Proc. of Symp. on Statistical Models and Turbulence, Lecture Notes in Physics*, vol. 12, p. 384, Springer.

WYNGAARD, J. C. & TENNEKES, H. 1970 *Phys. Fluids*, **13**, 1962.

YAGLOM, A. M. 1966 *Dokl. Akad. Nauk. SSR*, **116**, 49.